MOVA/MOSS: Two integrated software solutions for comprehensive Structural Health Monitoring of structures

Enrique García-Macías[a,*], Filippo Ubertini[a]

[a]*Department of Civil and Environmental Engineering, University of Perugia, Via G Duranti 93, Perugia 06125, Italy*

Abstract

Recent ground-breaking advances in sensing technologies, data processing, and structural identification have made Structural Health Monitoring (SHM) occupy a central place in Structural Engineering. Although the technological transfer to the industry is still in the early development stages, there is clear evidence that SHM-enabled condition-based maintenance of structures will soon supersede traditional periodic maintenance strategies. Among the existing solutions, ambient vibration-based SHM has become particularly popular owing to its minimum intrusiveness and global damage assessment capabilities. Nevertheless, it is well documented that local pathologies with limited impact over the stiffness of structures can be hardly detected by such techniques. As a solution, recent studies advocate the use of integrated monitoring systems, where data from heterogeneous sensor networks are simultaneously processed to achieve a comprehensive structural assessment. Despite the great advances of these systems reported by researchers, practitioners still find many difficulties to bring them to practice. In this light, this paper reports the development of two novel software solutions for long-term SHM of structures, MOVA and MOSS, that are intended to bridge this gap while also introducing new methodological and scientific advances. The developed software enables the online system identification and damage detection of structures, including vibration-based SHM and data fusion of heterogeneous sensing systems with an innovative automated anomaly detection algorithm. A case study of a permanent static/dynamic/environmental monitoring system installed in a monumental masonry palace, the Consoli Palace in Gubbio (Italy), is presented to illustrate the capabilities of MOVA/MOSS.

Keywords: Data fusion, Novelty Analysis, Operational Modal Analysis, Damage detection, Structural Health Monitoring, Unsupervised Learning

1. Introduction

In the last two decades, SHM has gained a leading role in the field of Structural Engineering. Recent tragic events, such as the Genoa bridge collapse in 2018, have highlighted the need to prioritize the maintenance of civil infrastructure in the political agenda. Civil engineering infrastructures are inevitably subjected to ageing degradation, as well as to a number of adverse external actions (e.g. extreme weather, earthquakes, or accidental loads). In particular, the last Infrastructure Report Card of the American Society of Civil Engineers (ASCE) released in 2017 [1] estimated that 39% of the 614387 American bridges are over 50 years old, and classified 9.1% of the bridges as structurally deficient or in poor conditions. Moreover, the ASCE's report estimated the corresponding rehabilitation costs at $123 billion. A similar picture emerges across Europe, where many of the bridges were built during the economic growth of the 1950s and, for instance, about 30% of the railway bridges exceed 100 years of age [2]. Nevertheless, despite large financial efforts have been dedicated to R&D actions in this field, the technology transfer has not been fully or successfully completed and SHM is still sparsely implemented in practice. Indeed, the last report of the European Joint Research Centre (JRC) [3] warned about the weak link between research and the wide-scale adoption of SHM technologies. To address these deficiencies, it is of pivotal importance to develop reliable and easy-to-use SHM solutions that facilitate practitioners' use of research breakthroughs.

Structural Health Monitoring aims to perform a diagnosis of the integrity of materials, structural components and assemblies constituting a structure [4]. This encompasses the application of Non-Destructive Testing (NDT) and damage identification tools and allows infrastructure managers to perform preventive condition-based maintenance, promote safety and maximize life expectancy. In essence, SHM involves long-term monitoring in order to track deviations in the structural response with respect to engineering-design specifications and past structural

*Corresponding author.
Email address: enrique.garciamacias@unipg.it (Enrique García-Macías)

performance. In this framework, ambient vibration-based SHM has received most attention owing to its minimal intrusiveness and fully non-destructive character [5]. These techniques exploit ambient acceleration records under normal operating conditions to extract the modal features of a system through output-only (Operational) Modal Analysis (OMA), namely natural frequencies, mode shapes, and damping ratios [6, 7]. The basic premise is that, since modal features are functions of the mass, stiffness, and energy dissipation mechanisms, damage in a structure can be inferred by tracking permanent variations in its modal parameters [8, 9]. Numerous recent works report the successful application of this technology to diverse structural typologies, including bridges [10], dams [11], buildings [12], stadiums [13], naval vessels [14], or aircraft structures [15]. Vibration-based SHM is also becoming increasingly popular for preventive conservation of Cultural Heritage (CH) structures. The monitoring of such structures must have a minimum impact on their architectural and cultural value, for which OMA-based SHM represents an ideal solution. In this context, plenty of successful applications can be found in the literature, including CH bridges [16, 17], towers [18, 19], churches [20], and buildings [21, 22].

Considerable research has been devoted to the development of automated OMA procedures [23–25]. These enable early detection of damage by tracking anomalies in time series of continuously identified modal features. Nonetheless, numerous papers have reported about the striking dependence of modal features on environmental (e.g. temperature, humidity, wind) and operational conditions (e.g. traffic level). For instance, Peeters and De Roeck [26] found variations up to 18% in the first four resonant frequencies of the well-known case study of the Z24-Bridge. This translates into daily and seasonal modal fluctuations that mask early stage damages. It follows that environmental effects must be filtered out through statistical pattern recognition and machine learning techniques [27]. In this context, the Z24 Bridge constitutes an important benchmark on which intensive research efforts have been exerted. The bridge was monitored during a nine-month period and, afterwards, artificial damage was introduced. Peeters and De Roeck [26] successfully detected the artificial damage by analysing the residuals between experimental resonant frequencies and statistical predictions obtained by an autoregressive model. Kullaa [28] and Yan and co-authors [29, 30] also worked on the Z24 Bridge and showed that damage can be also detected through control charts and Principal Component Analysis (PCA). Ubertini *et al*. [9] reported the damage detection of the bell-tower of the Basilica of San Pietro in Perugia during the 2016 Central Italy seismic sequence through long-term vibration-based SHM. To do so, the environmental effects were filtered out using Multiple Linear Regression (MLR) analysis and PCA, and the damage-induced anomalies in the residuals were analysed through control charts. Hu *et al*. [31] reported the vibration-based SHM of a prestressed-concrete box girder bridge in Berlin over 14 years. Through MLR filtering of the environmental effects, those authors found a progressive increase in the number of outliers in the control charts from 1.35% in 2000/2001 to 21.58% after 2008. Such reductions were consistent with measured decreases in the strain of the main pre-stressed tendon, what demonstrates the usefulness of vibration-based SHM for assessing progressive structural deterioration.

While highly effective in global structural assessment, vibration-based SHM may fail at detecting local defects with a limited impact on the stiffness. Hence, the use of integrated monitoring systems comprising diverse sensing solutions (e.g. dynamic, static, chemical) becomes imperative for effective local/global damage detection. Moreover, the assessment of environmental conditions is often critical for efficient data fusion and extraction of damage-sensitive features. The effects of environmental factors may dramatically vary depending on the type of construction material and the structural typology, so sensor layouts must be tailored for every specific case study. For instance, in masonry structures, positive correlations between environmental temperature and resonant frequencies are often observed [9, 32]. This is conceivably explained as the effect of the closing of superficial cracks or micro-cracks induced by thermal expansion of masonry. However, some other works such as the one by Gentile *et al*. [33] report the opposite behaviour. Those authors reported the SHM of the Milan Cathedral in Italy using both static (tilt meters and vibrating wire extensometers), environmental (hygrometers and temperature sensors) and dynamic sensors (seismometers). Their results showed a negative correlation between resonant frequencies and temperature, which was ascribed to the actions exerted by metallic tie-rods in the building. Negative frequency-temperature correlations are also common in reinforced-concrete and steel structures (see e.g. [34, 35]), which is usually ascribed to decreases in the material Young's modulus with increasing temperature. Nevertheless, likewise masonry structures, varying effects can be found depending on the specific structural typology, solar radiation, and temperature distribution (see e.g. [36, 37]).

Despite the advanced state of research, the number of software solutions that allow implementing SHM systems in practice is considerably limited. The most popular software programs for vibration-based SHM of structures are MACEC, LMS Test.Lab, and ARTeMIS. MACEC [38] is a MATLAB toolbox for OMA of structures developed by the Structural Mechanics Section of KU Leuven. This offers an extensive gallery of system identification methods for Ambient Vibration Testing (AVT) of structures, including, among others, Frequency Domain Decomposition (FDD), data-based and covariance-based Stochastic Subspace Identification (SSI), and Polyreference Least Squares Complex Frequency Domain method (p-LSCF). Nonetheless, this software does not allow performing continuous OMA and, therefore, cannot be directly applied to long-term vibration-based SHM. The

LMS Test.Lab Modal Analysis software [39] implements a very robust version of the p-LSCF method under the commercial name of PolyMAX although, alike MACEC, this software does not permit the implementation of long-term SHM systems. ARTeMIS [40] was developed by the company Structural Vibration Solutions A/S, funded in 1999 as a spin-off from Aalborg University in Denmark. This software is particularly well-suited for AVT of structures and, unlike the previous software programs, the most recent versions include a Damage Detection Plug-in with automated SSI and Hotelling's control charts. Nevertheless, ARTeMIS lacks the possibility of using statistical pattern recognition methods to filter out environmental effects and, therefore, it may be difficult to detect early-stage damage using this tool.

In view of the reported gap between research and professional practice, this paper introduces two new software programs for integrated SHM of structures, called MOVA and MOSS, Italian acronyms of "MOnitoraggio delle Vibrazioni Ambientali" (AVT) and "MOnitoraggio dello Stato di Salute" (SHM), respectively. MOVA focuses on AVT, while MOSS is dedicated to the online management of permanent integrated SHM systems. The latter includes automated OMA, frequency tracking, filtering of environmental effects, and fusion of heterogeneous sensor data. The data fusion capability of MOSS specifically lies in the possibility of performing pattern recognition using arbitrary combinations of predictors and estimators, including vibration and non-vibration data. Furthermore, an original algorithm for automated anomaly detection is introduced. In this way, once set up, the user has online access to a number of control charts assessing the performance of all those desired damage-sensitive features, and the system triggers an alarm (visual, sound, and/or by e-mail) when an anomaly is detected in any of them. Central to the development of MOVA/MOSS is the attention to ease of use and interpretability. Originally developed using MATLAB environment, MOVA and MOSS have been implemented in C++ providing a compact graphical user interface (GUI). In order to highlight the capabilities of MOVA/MOSS, this paper presents an application case study of the static/dynamic SHM of a monumental masonry palace, the Consoli Palace in Gubbio (Italy).

The remaining of the paper is organised as follows: Section 2 concisely describes the case study of the Consoli Palace. Section 3 outlines the theoretical background of vibration-based SHM. Section 4 describes the software architecture of MOVA/MOSS through an application case study of the Consoli Palace and, finally, Section 5 concludes the paper.

2. Application case study: The Consoli Palace in Gubbio, Italy

The Consoli Palace is the most emblematic monument of the city of Gubbio in Italy (Fig. 1 (a)). Erected between 1332 and 1349 to house the official courts, the Consoli Palace has hosted the Civic Museum of Gubbio since 1901. Including a bell-tower and a panoramic loggia, the building is 60 m high and has a rectangular plan of about 40×20 m. The palace features a Gothic style design with calcareous stone masonry, including an articulated internal distribution of volumes with thick masonry bearing walls and vaults as horizontal elements. Erected on the slope of the Ingino Mountain, the palace foundations are placed on two different levels with a drop of about 10 m. From the architectural point of view, the main façade is characterized by a distinctive fan-shaped staircase entrance and an arched portal.

As an exceptional example of a stiff historic building, the Consoli Palace has become the benchmark case study of several recent research projects. These include the Horizon 2020 European HERACLES project (2016-2018) devoted to enhancing resilience of historic buildings against harmful events, with emphasis on climate-change related effects. Within this project, a wide research programme was developed including diverse SHM methodologies and protocols for application to historic masonry palaces (see e.g. [22, 41, 42]). More recently, the Consoli Palace has also become the benchmark case study of a national Italian research project entitled "DETECT-AGING" and devoted to the monitoring of degradation effects on the structural safety of CH constructions. From these experiences, a considerable amount of monitoring data from different types of sensors has been collected, making the Consoli Palace an ideal example to illustrate the capabilities of MOVA/MOSS.

In this work, we focus on the static/dynamic/environmental monitoring of the Consoli Palace. Firstly, in order to characterize the modal features of the palace, an AVT with a moderately dense accelerometer network sketched in Fig. 1 (c) was conducted on May 4th 2017. This consisted of 9 uni-axial high sensitivity piezoelectric accelerometers (model PCB 393B12, ±0.50 g, and 10 V/g sensitivity) deployed on the three main floors of the palace at heights of 4.64, 18.89, and 29.77 m (labelled from TS1 to TS9). Afterwards, a permanent integrated SHM system has been installed in the Consoli Palace since July 2017, including 3 accelerometers, 2 crack meters, and 2 temperature sensors. Specifically, three PCB 393B12 accelerometers, labelled from PS1 to PS3, were deployed on the roof level of the palace. Two linear variable transducers (LVDTs) denoted as LVDT1 and LVDT2 (S-Series, measurement range 0-50 mm, resolution <0.3 μm) were installed across two major vertical cracks located on the second floor of the building. Finally, two K-type thermocouples were also installed close to each LVDTs. The sensors are connected to a NI CompactDAQ-9132 data acquisition system (processor 1.33 GHz Dual-Core Atom, 2 GB RAM, 16 GB SD storage, 4-Slot, Windows Embedded Standard 7 operating system) with a NI

9234 acceleration acquisition module (24-bit resolution, 102-dB dynamic range, and anti-aliasing filters) and a NI 9219 crack amplitude and temperature acquisition module (24-bit resolution, +-60V range, 100 S/s). The monitoring data were locally acquired and preliminarily processed through an in-house LabVIEW code, and stored in consecutive separate files containing 30 min-long recordings. Ambient accelerations were sampled at 100 Hz, while crack amplitudes and temperature values were sampled at 0.1 Hz. The data files were sent online through the Internet to a remove server located in the Laboratory of Structural Health Monitoring and Earthquake Engineering, where MOSS was used for automated SHM of the palace.

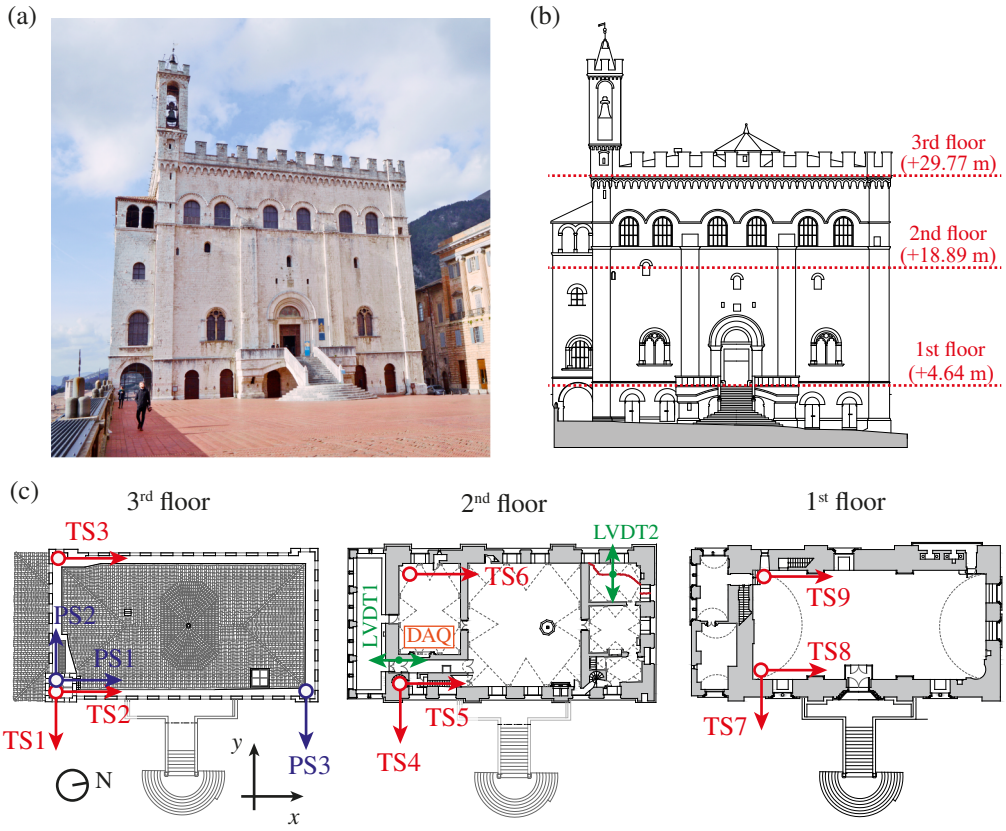

Figure 1: View of the Consoli Palace (a), elevation (b), and sketch of the structural monitoring system (c).

3. Theoretical background

MOVA and MOSS combine the experience on SHM of civil engineering structures accumulated by the research group during the last ten years. Some of the included routines have been previously tested in different structural typologies, specially bridges [24, 43] and CH structures [9, 22, 44].

3.1. Fundamentals of time-domain OMA methods

The differential equation of equilibrium of a dynamic system discretized into a finite element model (FEM) with n_2 degrees of freedom (DOFs) can be written in continuous state-space form as follows:

$$\begin{aligned} \dot{\mathbf{x}}(t) &= \mathbf{A}_C\mathbf{x}(t) + \mathbf{B}_C\mathbf{u}(t), \\ \dot{\mathbf{y}}(t) &= \mathbf{C}_C\mathbf{x}(t) + \mathbf{D}_C\mathbf{u}(t), \end{aligned} \tag{1}$$

where $\mathbf{A}_C \in \mathbb{R}^{2n_2\times 2n_2}$, $\mathbf{B}_C \in \mathbb{R}^{2n_2\times n_i}$, $\mathbf{C}_C \in \mathbb{R}^{l\times 2n_2}$, and $\mathbf{D}_C \in \mathbb{R}^{l\times n_i}$ are designated the state matrix, input matrix, output matrix, and direct transmission matrix, respectively. Vectors $\mathbf{x}(t) \in \mathbb{R}^{2n_2}$ and $\mathbf{y}(t) \in \mathbb{R}^{l}$ denote the state and observation vectors, respectively. The state vector $\mathbf{x}(t)$ contains the displacements and velocities of the DOFs of the system, while the observation vector $\mathbf{y}(t)$ contains a subset of l measured outputs. The first line in Eq. (1), called the state equation, relates n_i inputs (loads) applied to the system and contained in vector $\mathbf{u}(t) \in \mathbb{R}^{n_i}$ to the state vector $\mathbf{x}(t)$. On the other hand, the second line in Eq. (1) is called the observation equation and establishes a relation between the observation vector $\mathbf{y}(t)$ and the state vector $\mathbf{x}(t)$. The modal features of the system can

be extracted from the eigenvalue decomposition of the state matrix $\mathbf{A}_C$ as $\mathbf{A}_C = \boldsymbol{\Psi}\boldsymbol{\Lambda}_C\boldsymbol{\Psi}^{-1}$. Matrices $\boldsymbol{\Lambda}_C$ and $\boldsymbol{\Psi}$ containing the eigenvalues and eigenvectors of $\mathbf{A}_C$, respectively, present the following structure [45]:

$$\begin{aligned}
\boldsymbol{\Lambda}_C &= \begin{bmatrix} \boldsymbol{\Lambda} & 0 \\ 0 & \boldsymbol{\Lambda}^* \end{bmatrix}, \; \boldsymbol{\Psi} = \begin{bmatrix} \boldsymbol{\Theta} & \boldsymbol{\Theta}^* \\ \boldsymbol{\Theta}\boldsymbol{\Lambda} & \boldsymbol{\Theta}^*\boldsymbol{\Lambda}^* \end{bmatrix}, \\
\boldsymbol{\Lambda} &= \begin{bmatrix} \ddots & & \\ & \lambda_k & \\ & & \ddots \end{bmatrix}, \; \boldsymbol{\Theta} = \begin{bmatrix} \dots & \boldsymbol{\phi}_k & \dots \end{bmatrix}, \; k = 1, .., n_2
\end{aligned} \tag{2}$$

where $\bullet^*$ denotes complex conjugate. Parameters λ_k are related to the resonant frequencies (ω_k - natural frequencies in rad/s) and the modal damping ratios (ζ_k) of the system as:

$$\lambda_k = -\zeta_k\omega_k + \mathrm{i}\sqrt{1-\zeta_k^2}\omega_k, \tag{3}$$

with i denoting the imaginary unit. The mode shapes are represented in Eq. (2) by $\boldsymbol{\phi}_k \in \mathbb{R}^{n_2}$. However, since only a subset of l DOFs is measured, the observable modal matrix $\boldsymbol{\Phi} \in \mathbb{R}^{l \times n_2}$ is given by:

$$\boldsymbol{\Phi} = \mathbf{C}_C\boldsymbol{\Psi}. \tag{4}$$

In practice, recorded analogue signals are digitalized by an analogue-to-digital converter (A/D), so the available information is discrete in time. Such a process is conducted by sampling the signals at a certain sampling frequency $f_s = 1/\Delta t$, with Δt being the adopted sampling interval. Therefore, the time functions $\mathbf{x}(t)$ and $\mathbf{y}(t)$ in Eq. (1) must be replaced by their values at discrete time instants $k\Delta t$ with k being an integer, i.e. $\mathbf{y}_k = \mathbf{y}(k\Delta t)$, $\mathbf{x}_k = \mathbf{x}(k\Delta t)$. In addition, in the context of OMA, the system inputs in $\mathbf{u}(t)$ are unknown (unmeasured) and must be represented through stochastic processes. On this basis, the discrete stochastic state-space model reads:

$$\begin{aligned}
\mathbf{x}_{k+1} &= \mathbf{A}\mathbf{x}_k + \mathbf{w}_k, \\
\mathbf{y}_k &= \mathbf{C}\mathbf{x}_k + \mathbf{v}_k,
\end{aligned} \tag{5}$$

here, vectors $\mathbf{w}_k \in \mathbb{R}^{2n_2}$ and $\mathbf{v}_k \in \mathbb{R}^l$ represent white noise processes accounting for the effect of unknown outputs as well as the effects of process noise (modelling inaccuracies) and measurement noise, respectively. Both noise vectors are assumed to be zero-mean realizations of stochastic processes with the following correlation matrices:

$$E\left(\begin{bmatrix} \mathbf{w}_p \\ \mathbf{v}_p \end{bmatrix}\begin{bmatrix} \mathbf{w}_q^{\mathrm{T}} & \mathbf{v}_q^{\mathrm{T}} \end{bmatrix}\right) = \begin{bmatrix} \mathbf{Q} & \mathbf{S} \\ \mathbf{S}^{\mathrm{T}} & \mathbf{R} \end{bmatrix}\delta_{pq}, \tag{6}$$

where sub-indexes p and q denote generic time instants, δ_{pq} is the Kronecker delta, and E is the expected value operator.

It can be demonstrated that the eigenvectors of matrix $\mathbf{A}$ coincide with those of the continuous counterpart $\mathbf{A}_C$ and, since $\mathbf{C}$ equals $\mathbf{C}_C$, the modal matrix is given by Eq. (4) [46]. In addition, the eigenvalues of the discrete model μ_k are related to those of the continuous model λ_k as [46]:

$$\mu_k = e^{\lambda_k\Delta t} \Leftrightarrow \lambda_k = \frac{\ln(\mu_k)}{\Delta t}, \tag{7}$$

Therefore, the natural frequencies and model damping ratios can be readily obtained from the eigenvalues of matrix $\mathbf{A}$ using Eqs. (3) and (7).

An important property of stochastic state-space models regards the relation between the correlation matrix of the measurement records and the state-space matrices [45]:

$$\mathbf{R}_j = \mathbf{C}\mathbf{A}^{j-1}\mathbf{G}, \tag{8}$$

with $\mathbf{R}_j$ being the output correlation matrix for a time lag $\tau = j\Delta t$, and $\mathbf{G}$ being the next state-output covariance matrix given by:

$$\mathbf{G} = E\left[\mathbf{x}_{k+1}\mathbf{y}_k^{\mathrm{T}}\right]. \tag{9}$$

3.2. System identification

The software MOVA/MOSS offers four different system identification techniques, including two frequency-domain (EFDD and p-LSCF) and two time-domain identification techniques (COV-SSI and DATA-SSI).

3.2.1. Enhanced Frequency Domain Decomposition (EFDD)

The Frequency Domain Decomposition (FDD) method is based on the input/output relationship of linear time-invariant systems as [47]:

$$\mathbf{G}_{yy}(\omega) = \mathbf{H}(\omega)\mathbf{G}_{uu}(\omega)\mathbf{H}(\omega)^{\mathrm{H}}, \tag{10}$$

where $\bullet^{\mathrm{H}}$ denotes complex conjugate (Hermitian) transpose. Matrices $\mathbf{G}_{uu}(\omega) \in \mathbb{C}^{r_c \times r_c}$ and $\mathbf{G}_{yy}(\omega) \in \mathbb{C}^{l \times l}$ represent the Power Spectral Density (PSD) matrices of the inputs and outputs, respectively, with r_c being the number of inputs (references), and $\mathbf{H}(\omega) \in \mathbb{C}^{r_c \times l}$ is the Frequency Response Function (FRF) matrix. In practice, the PSDs are commonly computed using the Welch's method. Then, the singular value decomposition (SVD) of $\mathbf{G}_{yy}$ is performed as:

$$\mathbf{G}_{yy}(\omega_j) = \mathbf{U}_j\mathbf{S}_j\mathbf{U}_j^{\mathrm{H}}, \tag{11}$$

where $\mathbf{U}_j$ is an orthonormal matrix ($\mathbf{U}_j\mathbf{U}_j^{\mathrm{H}} = \mathbf{I}$) containing the singular vectors of $\mathbf{G}_{yy}(\omega_j)$, and $\mathbf{S}_j$ is a diagonal matrix holding the corresponding singular values (SVs). On this basis the resonant frequencies can be estimated by picking the peaks of the first SV, while the mode shapes are obtained as the first singular vector evaluated at the formerly picked frequency values.

The EFDD method represents an improved version of the FDD that allows to identify damping ratios and more accurate estimates of resonant frequencies. To do so, the singular value data around the resonance peaks are selected, typically according to a limit modal assurance criterion (MAC) value. Once selected, these spectrum segments are converted to the time domain in order to get auto-correlation functions for each mode. Finally, the corresponding resonant frequencies and damping ratios can be obtained by fitting the expression for the impulse response of a single-degree-of-freedom system. Alternatively, MOVA and MOSS implement the Single-Input-Multiple-Output (SIMO) version of the Ibrahim Time Domain (ITD) technique to extract the natural frequencies and damping ratios from the computed auto-correlation functions [48].

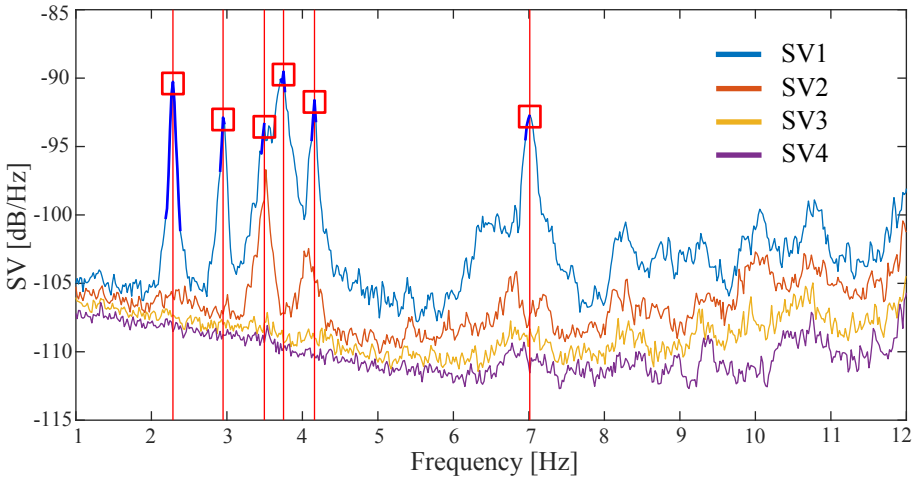

Figure 2: Dynamic identification of the Consoli Palace using EFDD in MOVA (SV plots and selected peaks).

Figure 2 presents the first four SVs of the spectral matrix calculated from the acceleration time-series recorded during the AVT of the Consoli Palace. These were calculated with the Welch's method using time segments with 2048 points, and Hanning windows with an overlapping of 50%. The application of the SVD decomposition to the spectral matrix evaluated at all the discrete frequencies between 0 and 12 Hz produces 9 SVs for each frequency. The spectrum of the first singular values exhibits six peaks that are associated with main modes of the Consoli Palace within the frequency band under analysis as further investigated in Section 4. The points of the singular value spectra are selected for the application of the ITD method using a limit for the MAC of 0.8.

3.2.2. Polyreference Least Squares Complex Frequency Domain method (p-LSCF)

The Polyreference Least Squares Complex Frequency Domain method (p-LSCF) is a parametric frequency-domain method developed by Peeters and Van der Auweraer [49]. The p-LSCF models the positive half-spectrum

matrix using a right-matrix fraction model as:

$$\mathbf{G}^{+}_{yy}(\omega_j) = \mathbf{B}(\omega_j)\left[\mathbf{A}(\omega_j)\right]^{-1} = \left[\sum_{r=0}^{p}\mathbf{B}_r\Omega_r(\omega_j)\right]\left[\sum_{r=0}^{p}\mathbf{A}_r\Omega_r(\omega_j)\right]^{-1}, \tag{12}$$

where matrices $\mathbf{B}_r$, $\mathbf{A}_r \in \mathbb{R}^{l\times l}$ are model parameter matrices to be determined, $\Omega_r(\omega_j)$ are polynomial basis functions, and p is the polynomial order. The p-LSCF model is expressed in the discrete z-domain (i.e. a frequency-domain model derived from a discrete-time model), so the polynomial basis functions take the form $\Omega_r(\omega_j) = e^{\mathrm{i}\omega_j\Delta t r}$. The method seeks matrices $\mathbf{B}_r$ and $\mathbf{A}_r$ that minimize in a non-linear least-squares sense the error matrix $\mathbf{E}^{NLS}(\omega_j) = \mathbf{G}^{+}_{yy}(\omega_j) - \hat{\mathbf{G}}^{+}_{yy}(\omega_j)$, which involves the difference between $\mathbf{G}^{+}_{yy}$ and the half-spectrum matrix $\hat{\mathbf{G}}^{+}_{yy}$ estimated from the measurement records. Nevertheless, the right multiplication of $\mathbf{E}^{NLS}(\omega_j)$ by matrix $\mathbf{A}(\omega_j)$ leads to more convenient linear least-squares equation errors as:

$$\mathbf{E}^{LS}(\omega_j) = \left[\sum_{r=0}^{p}\mathbf{B}_r\Omega_r(\omega)\right] - \hat{\mathbf{G}}^{+}_{yy}(\omega_j)\left[\sum_{r=0}^{p}\mathbf{A}_r\Omega_r(\omega)\right], \tag{13}$$

where $\mathbf{E}^{LS}(\omega_j) \in \mathbb{C}^{l\times l}$ contains the errors (E_{ij}) to be minimized. The minimization problem can be written in a more compact form after some transformations. In particular, an arbitrary line o of the error matrix at all the discrete frequency values from ω_1 to ω_{N_f} can be stacked in a matrix $\mathbf{E}^{LS}_o \in \mathbb{C}^{N_f\times l}$:

$$\mathbf{E}^{LS}_o(\boldsymbol{\beta}_o, \boldsymbol{\alpha}) = \begin{bmatrix} E_{o1}(\omega_1) & \dots & E_{ol}(\omega_1) \\ E_{o1}(\omega_2) & \dots & E_{ol}(\omega_2) \\ \dots & \dots & \dots \\ E_{o1}(\omega_{N_f}) & \dots & E_{ol}(\omega_{N_f}) \end{bmatrix} = \begin{bmatrix}\mathbf{X}_o & \mathbf{Y}_o\end{bmatrix}\begin{bmatrix}\boldsymbol{\beta}_o \\ \boldsymbol{\alpha}\end{bmatrix}, \tag{14}$$

with

$$\begin{aligned} \boldsymbol{\Omega}(\omega_j) &= \begin{bmatrix}\Omega_0(\omega_j)\,\Omega_2(\omega_j)\,\dots\,\Omega_p(\omega_j)\end{bmatrix} \in \mathbb{C}^{p+1}, \\ \mathbf{Y}_o &= \begin{bmatrix} \Omega_0(\omega_1)\hat{\mathbf{S}}^{+}_{yyo} & \Omega_1(\omega_1)\hat{\mathbf{S}}^{+}_{yyo} & \dots & \Omega_p(\omega_1)\hat{\mathbf{S}}^{+}_{yyo} \\ & \vdots & \dots & \\ \Omega_0(\omega_{N_f})\hat{\mathbf{S}}^{+}_{yyo} & \Omega_1(\omega_{N_f})\hat{\mathbf{S}}^{+}_{yyo} & \dots & \Omega_p(\omega_{N_f})\hat{\mathbf{S}}^{+}_{yyo} \end{bmatrix} \in \mathbb{C}^{N_f\times l(p+1)}, \\ \mathbf{X}_o &= \begin{bmatrix}\boldsymbol{\Omega}(\omega_1) \\ \vdots \\ \boldsymbol{\Omega}(\omega_{n_f})\end{bmatrix} \in \mathbb{C}^{N_f\times(p+1)},\ \boldsymbol{\beta}_o = \begin{bmatrix}\mathbf{B}_{0o} \\ \mathbf{B}_{1o} \\ \dots \\ \mathbf{B}_{po}\end{bmatrix} \in \mathbb{R}^{(p+1)\times l},\ \boldsymbol{\alpha} = \begin{bmatrix}\mathbf{A}_0 \\ \mathbf{A}_1 \\ \dots \\ \mathbf{A}_p\end{bmatrix} \in \mathbb{R}^{l(p+1)\times l}, \end{aligned} \tag{15}$$

where $\hat{\mathbf{S}}^{+}_{yyo}$ and $\mathbf{B}_{ro}$ represent the o lines of matrices $\hat{\mathbf{S}}^{+}_{yy}$ and $\mathbf{B}_r$, respectively. Finally, a scalar cost function can be constructed as the sum of the squared elements of the error matrix as:

$$\varepsilon(\boldsymbol{\beta}_o, \boldsymbol{\alpha}) = \sum_{o=1}^{l}\mathrm{tr}\left\{\mathbf{E}_o(\boldsymbol{\beta}_o, \boldsymbol{\alpha})^{\mathrm{H}}\mathbf{E}_o(\boldsymbol{\beta}_o, \boldsymbol{\alpha})\right\} = \sum_{o=1}^{l}\mathrm{tr}\left\{\begin{bmatrix}\boldsymbol{\beta}_o^{\mathrm{T}} & \boldsymbol{\alpha}^{\mathrm{T}}\end{bmatrix}\begin{bmatrix}\mathbf{R}_o & \mathbf{S}_o \\ \mathbf{S}_o^{T} & \mathbf{T}_o\end{bmatrix}\begin{bmatrix}\boldsymbol{\beta}_o \\ \boldsymbol{\alpha}\end{bmatrix}\right\}, \tag{16}$$

with $\mathbf{R}_o = \mathrm{Re}(\mathbf{X}_o^{\mathrm{H}}\mathbf{X}_o) \in \mathbb{R}^{(p+1)\times(p+1)}$, $\mathbf{S}_o = \mathrm{Re}(\mathbf{X}_o^{\mathrm{H}}\mathbf{Y}_o) \in \mathbb{R}^{(p+1)\times l(p+1)}$, $\mathbf{T}_o = \mathrm{Re}(\mathbf{Y}_o^{\mathrm{H}}\mathbf{Y}_o) \in \mathbb{R}^{l(p+1)\times l(p+1)}$, and tr denoting the trace operator. The unknown model parameters in $\mathbf{B}_r$ and $\mathbf{A}_r$ can be obtained by forcing the derivatives of the cost function with respect to $\boldsymbol{\alpha}$ and $\boldsymbol{\beta}_o$ to be zero. This leads to the following reduced system of equations:

$$\begin{aligned} &2(\mathbf{R}_o\boldsymbol{\beta}_o + \mathbf{S}_o\boldsymbol{\alpha}) = \mathbf{0} \Leftrightarrow \boldsymbol{\beta}_o = -\mathbf{R}_o^{-1}\mathbf{S}_o\boldsymbol{\alpha}, \\ &2\sum_{o=1}^{l}\left(\mathbf{T}_o - \mathbf{S}_o^{\mathrm{T}}\mathbf{R}_o^{-1}\mathbf{S}_o\right)\boldsymbol{\alpha} = 0 \Leftrightarrow \mathbf{M}\boldsymbol{\alpha} = 0, \end{aligned} \tag{17}$$

where matrix $\mathbf{M} \in \mathbb{C}^{l(p+1)\times l(p+1)}$ can be computed from the output half-spectrum matrix estimated from the measurement records. In order to avoid the trivial solution of the previous equation ($\boldsymbol{\alpha} = \mathbf{0}$), a constraint has to be imposed. This is typically conducted by forcing either $\mathbf{A}_o$ or $\mathbf{A}_p$ to be the identity matrix. In particular, clearer

stabilization diagrams have been reported to be found when $\mathbf{A}_o = \mathbf{I}$ [6]. Then, the resolution of the system of equations reads:

$$\mathbf{M}\boldsymbol{\alpha} = \mathbf{0} \Leftrightarrow \left[\begin{array}{c|c} \mathbf{M}_{aa} & \mathbf{M}_{ab} \\ \hline \mathbf{M}_{ba} & \mathbf{M}_{bb} \end{array}\right]\left[\begin{array}{c} \mathbf{I} \\ \hline \boldsymbol{\alpha}_b \end{array}\right] = \left[\begin{array}{c} \mathbf{0} \\ \hline \mathbf{0} \\ \vdots \\ \mathbf{0} \end{array}\right] \Leftrightarrow \boldsymbol{\alpha}_b = -\mathbf{M}_{bb}^{-1}\mathbf{M}_{ba} \Leftrightarrow \boldsymbol{\alpha} = \left[\begin{array}{c} \mathbf{I} \\ -\mathbf{M}_{bb}^{-1}\mathbf{M}_{ba} \end{array}\right], \tag{18}$$

where $\mathbf{M}_{ba}$ contains the first l columns and the last pl lines of $\mathbf{M}$, $\mathbf{M}_{bb}$ contains the last pl columns and rows of $\mathbf{M}$, and $\boldsymbol{\alpha}_b$ contains the last pl rows of $\boldsymbol{\alpha}$. Once matrix $\boldsymbol{\alpha}$ is determined, matrix $\boldsymbol{\beta}_o$ is directly obtained using the relation between $\boldsymbol{\alpha}$ and $\boldsymbol{\beta}_o$ in Eq. (17). With this step, the model parameter matrices $\mathbf{A}_r$ and $\mathbf{B}_r$ are determined and the identification problem is solved. Then, the modal features can be obtained through the transposition equations from right matrix-fraction models to state-space models, leading to the following state-space matrices [50]:

$$\begin{aligned}
\mathbf{A}_C &= \begin{bmatrix} -\mathbf{A}_p^{-1}-\mathbf{A}_{p-1} & -\mathbf{A}_p^{-1}-\mathbf{A}_{p-2} & \dots & -\mathbf{A}_p^{-1}-\mathbf{A}_1 & -\mathbf{A}_p^{-1}-\mathbf{A}_0 \\ \mathbf{I} & \mathbf{0} & \dots & \mathbf{0} & \mathbf{0} \\ \vdots & \ddots & \dots & \vdots & \vdots \\ \mathbf{0} & \mathbf{0} & \dots & \mathbf{I} & \mathbf{0} \end{bmatrix}, \\
\mathbf{B}_C &= \begin{bmatrix} \mathbf{A}_p^{-1} \\ \mathbf{0} \end{bmatrix}, \\
\mathbf{C}_C &= \begin{bmatrix} \mathbf{B}_{p-1}-\mathbf{B}_p\mathbf{A}_p^{-1}\mathbf{A}_{p-1} & \dots & \mathbf{B}_0-\mathbf{B}_p\mathbf{A}_p^{-1}\mathbf{A}_0 \end{bmatrix}, \\
\mathbf{D}_C &= \mathbf{B}_p\mathbf{A}_p^{-1}.
\end{aligned} \tag{19}$$

Finally, the modal features can be readily determined through the eigenvalue decomposition of matrix $\mathbf{A}$. At this point, separation of physical and spurious modes becomes crucial. This is commonly performed through stabilization diagrams representing the modal parameters estimated considering p-LSCF models with increasing polynomial orders p. Figure 3 shows the stabilization diagram obtained using the p-LSCF method in MOVA for the ambient vibration dataset recorded during the AVT of the Consoli Palace. To do so, the cross half-spectra of the nine time series of ambient vibrations were obtained using the Welch's method considering time segments with 2048 points and 50% overlap. Afterwards, the model conversion in Eq. (19) was constructed by adopting polynomial orders between 20 and 120. It is noted in Fig. 3 that six clear columns of stable poles are found at frequency values corresponding to the main natural frequencies of the Consoli Palace in the considered frequency range. These results exemplify one of the main advantages of the p-LSCF method, which regards the generation of very clear stabilization diagrams. Indeed, it has been previously reported in the literature that most of the spurious poles appear with negative damping ratios when using the p-LSCF method, thereby they are directly eliminated before constructing the stabilization diagram [45].

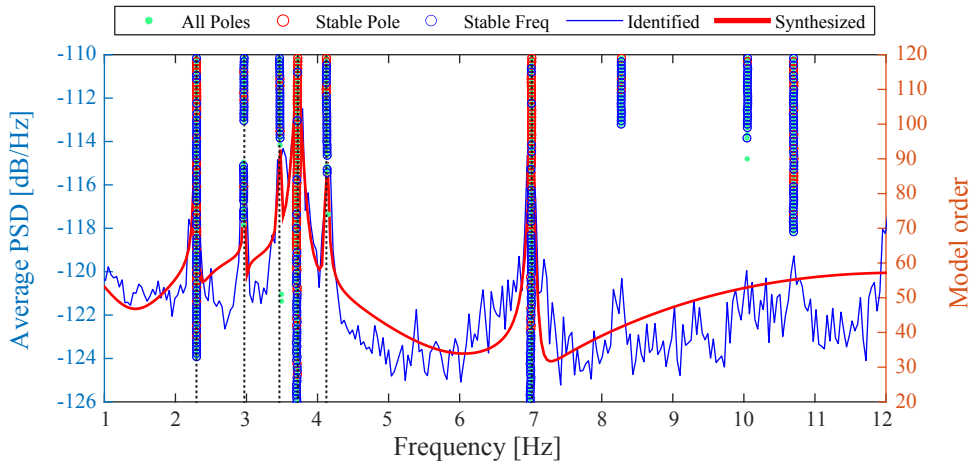

Figure 3: Dynamic identification of the Consoli Palace using p-LSCF in MOVA (stabilization diagram).

3.2.3. Stochastic Subspace Identification

The developed software includes two time-domain SSI methods, namely the Covariance driven SSI method (SSI-COV) and the data-driven SSI method (SSI-DATA).

SSI-COV

The SSI-COV method identifies a stochastic state-space model from the output covariance matrix (or correlation, as the mean of the signals is assumed to be zero). It starts by computing the output correlation matrix for positive time lags varying from Δt to $(2j_b - 1)\Delta t$ represented by $\mathbf{R}_1$ to $\mathbf{R}_{2j_b-1}$. Afterwards, the covariance matrix is organized in a lj_b-by-lj_b block Toeplitz matrix (sketched in Fig. 4) as:

$$\mathbf{T}_{1|_{j_b}} = \begin{bmatrix} \mathbf{R}_{j_b} & \mathbf{R}_{j_b-1} & \dots & \mathbf{R}_1 \\ \mathbf{R}_{j_b+1} & \mathbf{R}_{j_b} & \dots & \mathbf{R}_2 \\ \dots & \dots & \dots & \dots \\ \mathbf{R}_{2j_b-1} & \mathbf{R}_{2j_b-2} & \dots & \mathbf{R}_{j_b} \end{bmatrix}. \tag{20}$$

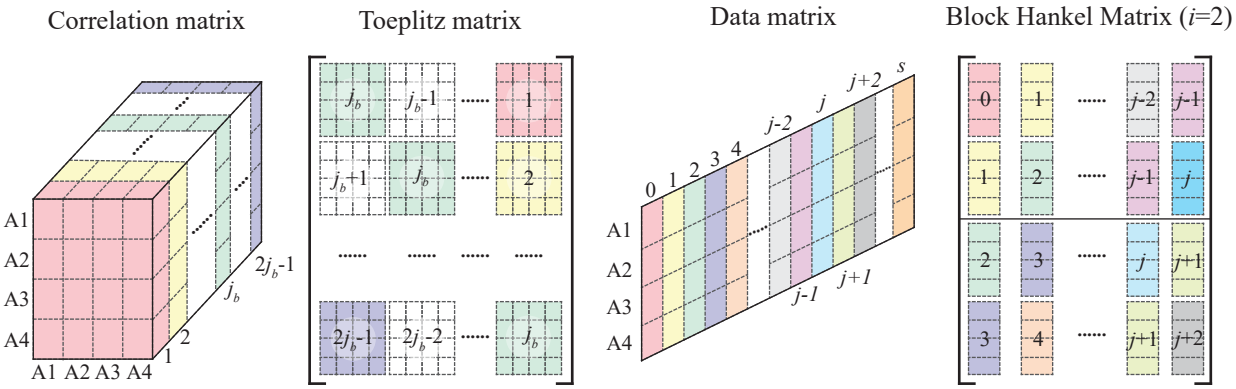

Figure 4: Schematic representation of the construction of the Toeplitz matrix and block Hankel matrix for SSI-COV and SSI-DATA, respectively.

Applying the factorization property of the correlation matrix in Eq. (8) to all the R_j matrices stored in the Toeplitz matrix, $T_{1|_{j_b}}$ can be decomposed in the product of the following matrices:

$$\mathbf{T}_{1|_{j_b}} = \begin{bmatrix} \mathbf{C} \\ \mathbf{CA} \\ \dots \\ \mathbf{CA}^{j_b-1} \end{bmatrix} \begin{bmatrix} \mathbf{A}^{j_b-1}\mathbf{G} & \dots & \mathbf{AG} & \mathbf{G} \end{bmatrix} = \mathbf{O\Gamma}. \tag{21}$$

The second equality in Eq. (21) defines the following matrices: $\mathbf{O}$- extended observability matrix; and $\mathbf{\Gamma}$- reversed extended stochastic controllability matrix. The first one is a column of j_b blocks with dimensions l-by-n (n is the dimension of the state-space model). The second one is formed by j_b n-by-l matrices organized in a row. According to the previous equation, the Toeplitz matrix results from the product of a matrix with n columns by a matrix with n rows. Therefore, if $n < lj_b$, the rank of $T_{1|_{j_b}}$ is equal to n. Then, the SVD of the block Toeplitz matrix is calculated:

$$\mathbf{T}_{1|_{j_b}} = \mathbf{USV}^{\mathrm{T}} = \begin{bmatrix} \mathbf{U}_1 & \mathbf{U}_2 \end{bmatrix} \begin{bmatrix} \mathbf{S}_1 & \mathbf{0} \\ \mathbf{0} & \mathbf{0} \end{bmatrix} \begin{bmatrix} \mathbf{V}_1^{\mathrm{T}} \\ \mathbf{V}_2^{\mathrm{T}} \end{bmatrix} = \mathbf{U}_1\mathbf{S}_1\mathbf{V}_1^{\mathrm{T}}. \tag{22}$$

The number of non-zero SVs gives the rank of the decomposed matrix, which, in this case, coincides with n (assuming $n < lj_b$), the dimension of the state-space matrix $\mathbf{A}$. The comparison of Eqs. (21) and (22) shows that the observability and the controllability matrices can be calculated from the outputs of the SVD using the following partition of the singular values matrix:

$$\begin{aligned} \mathbf{O} &= \mathbf{U}_1\mathbf{S}_1^{1/2}, \\ \mathbf{\Gamma} &= \mathbf{S}_1^{1/2}\mathbf{V}_1^{\mathrm{T}}. \end{aligned} \tag{23}$$

Once the observability and controllability matrices are obtained, the identification of the state-space model matrices $\mathbf{A}$ and $\mathbf{C}$ is straightforward. On one hand, matrix $\mathbf{C}$ can be extracted from the first l lines of the observability matrix. On the other hand, the state matrix $\mathbf{A}$ can be computed according to different approaches. The developed software utilizes the Balanced Realization (BR) method which exploits the shift structure of the observability matrix, that is [45]:

$$\begin{bmatrix} \mathbf{C} \\ \mathbf{CA} \\ \dots \\ \mathbf{CA}^{j_b-2} \end{bmatrix} \mathbf{A} = \begin{bmatrix} \mathbf{CA} \\ \mathbf{CA}^2 \\ \dots \\ \mathbf{CA}^{j_b-1} \end{bmatrix} \Leftrightarrow \mathbf{A} = \begin{bmatrix} \mathbf{C} \\ \mathbf{CA} \\ \dots \\ \mathbf{CA}^{j_b-2} \end{bmatrix}^{\dagger} \begin{bmatrix} \mathbf{C} \\ \mathbf{CA}^2 \\ \dots \\ \mathbf{CA}^{j_b-1} \end{bmatrix} = \mathbf{O}^{to\dagger} \mathbf{O}^{bo}, \tag{24}$$

where $\mathbf{O}^{to}$ contains the first $l(j_b - 1)$ lines of $\mathbf{O}$, and $\mathbf{O}^{bo}$ contains the last $l(j_b - 1)$ lines of $\mathbf{O}_{j_b}$. The symbol † represents the Moore-Penrose pseudo-inverse.

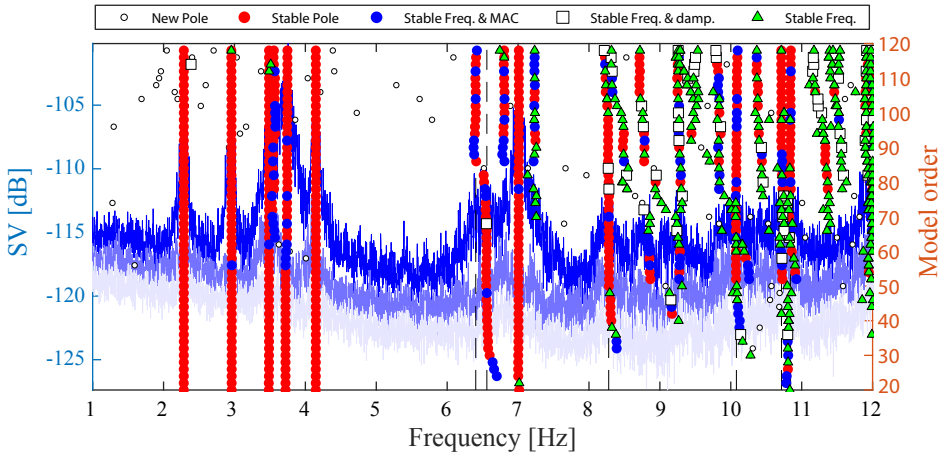

Figure 5: Dynamic identification of the Consoli Palace using SSI-COV in MOVA (stabilization diagram).

Figure 5 shows the stabilization diagram obtained using the SSI-COV method in MOVA for the ambient vibration dataset recorded during the AVT of the Consoli Palace. To do so, *jb* has been assumed as 70, resulting in a $70 \cdot 9 \times 70 \cdot 9$ Toeplitz matrix. Then, matrices $\mathbf{O}$, $\mathbf{\Gamma}$, $\mathbf{A}$ and $\mathbf{C}$ and then the modal parameters are estimated considering an odd number of singular values and vectors varying from 20 to 120. Similarly to the previous analyses, it is noted in Fig. 5 that six clear columns of stable poles are found at frequency values corresponding to the main natural frequencies of the Consoli Palace in the considered frequency range.

SSI-DATA

Data-driven stochastic subspace identification (SSI-DATA) is similar to SSI-COV, but identifies the state sequence before the estimation of the state-space matrices. Data-driven SSI consists of the following steps: (a) construction of the block Hankel matrix of the measurements, H_i; (b) computation of the projection matrix, P_i; (c) estimation of the observability matrix, Γ_i; and (d) extraction of the modal parameters estimates from matrix Γ_i. The block Hankel matrix (sketched in Fig. 4) is defined as:

$$\mathbf{H}_i = \frac{1}{\sqrt{j}} \left[\begin{array}{cccc} \mathbf{y}(0) & \mathbf{y}(1) & \dots & \mathbf{y}(j-1) \\ \mathbf{y}(1) & \mathbf{y}(2) & \dots & \mathbf{y}(j) \\ \vdots & \vdots & \ddots & \vdots \\ \mathbf{y}(i-1) & \mathbf{y}(i) & \dots & \mathbf{y}(i+j-2) \\ \hline \mathbf{y}(i) & \mathbf{y}(i+1) & \dots & \mathbf{y}(i+j-1) \\ \mathbf{y}(i+1) & \mathbf{y}(i+2) & \dots & \mathbf{y}(i+j) \\ \vdots & \vdots & \ddots & \vdots \\ \mathbf{y}(2i-1) & \mathbf{y}(2i) & \dots & \mathbf{y}(2i+j-2) \end{array}\right] = \left[\begin{array}{c} \mathbf{Y}_{0|i-1} \\ \hline \mathbf{Y}_{i|2i-1} \end{array}\right] = \left[\begin{array}{c} \mathbf{Y}_p \\ \hline \mathbf{Y}_f \end{array}\right], \tag{25}$$

where $2i$ and j, with $j \leq s - 2i + 1$, are user-defined quantities representing the number of output block rows and the number of columns of matrix $\mathbf{H}_i$, respectively. The block Hankel matrix in Eq. (25) is subdivided into two

sub-matrices, named as $\mathbf{Y}_p$ and $\mathbf{Y}_f$, which are usually referred to as past and future output block matrices. The identification of the Kalman filter state sequences and, as a consequence, of the state-space matrices is based on the orthogonal projection of the row space of the future outputs on the row space of the past outputs:

$$\mathbf{P}_i = \mathbf{Y}_f/\mathbf{Y}_p = \mathbf{Y}_f\mathbf{Y}_p^{\mathrm{T}}\left(\mathbf{Y}_p\mathbf{Y}_p^{\mathrm{T}}\right)^{\dagger}\mathbf{Y}_p, \tag{26}$$

which can be efficiently computed by the LQ factorization of the block Hankel matrix of the outputs. The main theorem of DATA-SSI states that the projection matrix $\mathbf{P}_i$ can be factorized into the product of the observability matrix $\mathbf{O}_i$ and the Kalman filter state sequence $\hat{\mathbf{S}}_i$:

$$\mathbf{P}_i = \mathbf{O}_i\hat{\mathbf{S}}_i, \tag{27}$$

where $\hat{\mathbf{S}}_i$ is a matrix containing Kalman filter estimates of the state vector at different time steps. Similarly, the projection matrix $\mathbf{P}_{i-1}$ can be obtained as:

$$\left[\begin{array}{c}\mathbf{Y}_{0|i-1}\\ \hline \mathbf{Y}_{i|i}\\ \hline \mathbf{Y}_{i+1|2i-1}\end{array}\right] = \left[\begin{array}{c}\mathbf{Y}_{0|i}\\ \hline \mathbf{Y}_{i+1|2i-1}\end{array}\right] = \left[\begin{array}{c}\mathbf{Y}_p^+\\ \mathbf{Y}_f^-\end{array}\right] \Leftrightarrow \mathbf{P}_{i-1} = \mathbf{Y}_f^-/\mathbf{Y}_p^+, \tag{28}$$

where $\mathbf{Y}_p^+$ is the past output with one extra block row, while $\mathbf{Y}_f^-$ is the future output matrix without the first block row $\mathbf{Y}_{i|i}$. The observability matrix $\mathbf{O}_i$ can be estimated from the SVD of matrix $\mathbf{W}_1\mathbf{P}_i\mathbf{W}_2$:

$$\mathbf{W}_1\mathbf{P}_i\mathbf{W}_2 = \left[\begin{array}{cc}\mathbf{U}_1 & \mathbf{U}_2\end{array}\right]\left[\begin{array}{cc}\mathbf{\Sigma}_1 & \mathbf{0}\\ \mathbf{0} & \mathbf{0}\end{array}\right]\left[\begin{array}{c}\mathbf{V}_1^{\mathrm{T}}\\ \mathbf{V}_2^{\mathrm{T}}\end{array}\right] = \mathbf{U}_1\mathbf{\Sigma}_1\mathbf{U}_1^{\mathrm{T}} \tag{29}$$

According to the Canonical Variate Analysis (CVA) method, the weighting matrices $\mathbf{W}_1$ and $\mathbf{W}_2$ take the form $\mathbf{W}_1 = \left((1/j)\mathbf{Y}_f\mathbf{Y}_f^{\mathrm{T}}\right)^{-1/2}$ and $\mathbf{W}_2 = \mathbf{I}$. Then, the observability matrix $\mathbf{O}_i$ and the Kalman filter state sequence $\hat{\mathbf{S}}_i$ can be computed as:

$$\begin{aligned}\mathbf{O}_i &= \mathbf{U}_1\mathbf{\Sigma}_1^{1/2},\\ \hat{\mathbf{S}}_i &= \mathbf{O}_i^{\dagger}\mathbf{P}_i.\end{aligned} \tag{30}$$

A similar factorization can be applied to $\mathbf{P}_{i-1}$:

$$\mathbf{P}_{i-1} = \mathbf{O}_i^{\uparrow}\hat{\mathbf{S}}_{i_1} \Leftrightarrow \hat{\mathbf{S}}_{i+1} = \left(\mathbf{O}_i^{\uparrow}\right)^{\dagger}\mathbf{P}_{i-1}, \tag{31}$$

where $\mathbf{O}_i^{\uparrow}$ can be directly obtained from $\mathbf{O}_i$ by deleting the last l rows. Finally, the state-space matrices $\mathbf{A}$ and $\mathbf{C}$ are obtained in a least squares sense as [51]:

$$\left[\begin{array}{c}\mathbf{A}\\ \mathbf{C}\end{array}\right] = \left[\begin{array}{c}\hat{\mathbf{S}}_{i+1}\\ \mathbf{Y}_{i|i}\end{array}\right]\hat{\mathbf{S}}_i^{\dagger}. \tag{32}$$

3.3. Automated system identification

The current version of MOSS allows performing automated system identification using SSI. To do so, the code includes the automation procedure introduced in reference [24] and concisely overviewed herein. This comprises the following steps: (a) modal identification for different values i and j of the number of rows and columns of the Toeplitz/Hankel matrices, respectively; (b) noise modes elimination; and (c) clustering analysis.

(a) Iterative modal identification

A total number of N SSI analyses are performed considering values of j and i varying within certain user-defined intervals $[j_{min}, j_{max}]$ and $[i_{min}, i_{max}]$ and steps Δj and Δi, respectively. Specific rules for setting adequate values of i_{min} i_{max}, j_{min}, j_{max}, Δi and Δj can be found in reference [24], and are included as default parameters in MOSS. This procedure results in a set of M poles, whose modal information can be organized in matrix form as:

$$\begin{aligned}\mathbf{f} &= [f_1\ f_2\ \ldots\ f_M]^{\mathrm{T}},\\ \boldsymbol{\zeta} &= [\zeta_1\ \zeta_2\ \ldots\ \zeta_M]^{\mathrm{T}},\\ \mathbf{\Theta} &= [\mathbf{\Theta}_1\ \mathbf{\Theta}_2\ \ldots\ \mathbf{\Theta}_M],\end{aligned} \tag{33}$$

where f_m, ζ_m, and $\mathbf{\Theta}_m$ denote the frequency, damping, and mode shape vector of an arbitrary m-th mode, $m = 1, 2, \ldots, M$.

(b) Noise modes elimination

Noise modes elimination is performed by a similar approach to the interpretation of stabilization diagrams, but accounting for variations of both j and i. To discern between noise modes and physical ones, a vector $\mathbf{c} = [c_1\, c_2\, \dots\, c_M]^{\mathrm{T}}$ is computed with components c_m, $m = 1, 2, \dots, M$, given by:

$$c_m = \begin{cases} -1 + \sum_{l=1}^{M} \delta_{lm}, & \text{if} \quad \zeta_m \in [0\, \zeta_{max}] \\ 0, & \text{if} \quad \zeta_m \notin [0\, \zeta_{max}] \end{cases} \tag{34}$$

with

$$\begin{aligned} \delta_{lm} &= \begin{cases} 1, & \text{if} \quad \Delta f_{lm} \leq \epsilon_f,\, \Delta\zeta_{lm} \leq \epsilon_\zeta,\, 1 - MAC_{lm} \leq \epsilon_{MAC} \\ 0, & \text{otherwise} \end{cases} \\ \Delta f_{lm} &= \frac{|f_l - f_m|}{f_m},\ \Delta\zeta_{lm} = \frac{|\zeta_l - \zeta_m|}{\zeta_m},\ MAC_{lm} = MAC(\boldsymbol{\Theta}_l, \boldsymbol{\Theta}_m), \end{aligned} \tag{35}$$

where ζ_{max} is the maximum reasonable value for the damping ratio of the physical modes (≈5-10% depending on the structural typology), $MAC(\boldsymbol{\Theta}_l, \boldsymbol{\Theta}_m)$ is the MAC value between modes Θ_l and Θ_m, and ϵ_f, ϵ_ζ, and ϵ_{MAC} are user-defined tolerances. An arbitrary component c_m represents the number of modes, among all the M identified ones, which have similar modal features to those of the m-th mode. Therefore, the m-th mode is said to be stable when it is similar in terms of frequency, damping, and mode shape to a minimum number N_{min} of other modes, i.e. $c_m \geq N_{min}$. A value of $N_{min} = N/10$ is selected as a compromise for eliminating most of the noise modes without cancelling the physical ones [24]. Then, the number of stable poles can be readily obtained computing a vector $\mathbf{S}$:

$$\begin{aligned} \mathbf{S} &= [S_1\, S_2\, \dots\, S_M]^{\mathrm{T}}, \\ S_m &= \begin{cases} 1, & \text{if} \quad c_m \geq N_{min} \\ 0, & \text{otherwise} \end{cases} \end{aligned} \tag{36}$$

whose components assign 0 and 1 to unstable and stable modes, respectively. Hence, the total number of stable modes, P, simply reads $P = \sum_{l=1}^{M} S_l$. The vectors of stable frequencies $\mathbf{f}^s$ and damping ratios $\boldsymbol{\zeta}^s$, and the matrix of stable mode shapes $\boldsymbol{\Theta}^s$ can be extracted as:

$$\begin{aligned} \mathbf{f}^s &= \mathbf{HE}\,\mathbf{f} = [f_1\, f_2\, \dots\, f_P]^{\mathrm{T}}, \\ \boldsymbol{\zeta}^s &= \mathbf{HE}\,\boldsymbol{\zeta} = [\zeta_1\, \zeta_2\, \dots\, \zeta_P]^{\mathrm{T}}, \\ \boldsymbol{\Theta}^s &= \left(\mathbf{HE}\,\boldsymbol{\Theta}^{\mathrm{T}}\right)^{\mathrm{T}} = [\boldsymbol{\Theta}_1\, \boldsymbol{\Theta}_2\, \dots\, \boldsymbol{\Theta}_P], \end{aligned} \tag{37}$$

where $\mathbf{HE}$ is a $P \times M$ matrix whose non-zero components are $HE_{p,\pi_p} = 1$, $p = 1, 2, \dots, P$, with $\pi_1, \pi_2, \dots, \pi_p$ being the positions of the non-zero terms of vector $\mathbf{S}$.

(c) Clustering analysis

An agglomerate hierarchical clustering algorithm is implemented to automate the interpretation of the SSI outputs from the previous steps. Such an analysis is aimed at grouping the P stable modes into a set of homogeneous data clusters pertaining to the same structural mode. The algorithm starts by generating a permutation vector $\mathbf{v} = [v_1, v_2, \dots, v_P]^{\mathrm{T}}$, containing the elements of vector $\mathbf{p} = [1, 2, \dots, P]^{\mathrm{T}}$ in a random order. There follows an iterative procedure composed of P steps sketched in Fig. 6. At the first step, the v_1-th mode is considered as the first cluster seed $C_1^1 = \{v_1\}$, where C_1^1 represents cluster C_1 evaluated at step number 1 (superscript 1). The next $P - 1$ steps work in a similar way. Let us focus on a generic q-th step, at which a certain number r of clusters will already exist. In order to compare the v_q-th mode and a cluster C_j, $j \in [1, ..., r]$, a similarity rule is defined as:

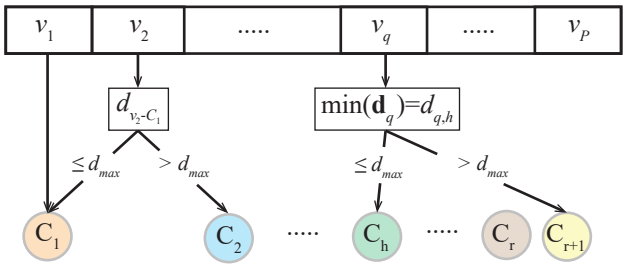

Figure 6: Graphical sketch of the hierarchical clustering approach.

$$d_{v_q-C_j} = \frac{\left| f^s_{v_q} - \overline{f}_{C_j} \right|}{\overline{f}_{C_j}} + 1 + MAC(\boldsymbol{\Theta}^s_{v_q}, \overline{\boldsymbol{\Theta}}_{C_j}), \tag{38}$$

where $\overline{f}_{C_j}$ and $\overline{\boldsymbol{\Theta}}_{C_j}$ denote the mean values of the frequencies and mode shapes of the poles composing cluster C_j, respectively, while $f^s_{v_q}$ and $\boldsymbol{\Theta}^s_{v_q}$ are the frequency and the mode shape of the v_q-th mode, respectively. Then, the similarities between the v_q-th mode and the r clusters are arranged in a similarity vector $\mathbf{d}_q$ as:

$$\mathbf{d}_q = \left[d_{v_q-C_1}, d_{v_q-C_2}, \ldots, d_{v_q-C_r} \right]^{\mathrm{T}}, \tag{39}$$

and the following rule is applied:

$$\begin{aligned} &\text{if } d_{q,h} = \min(\mathbf{d}_q) \leq d_{max} \Rightarrow C^q_h = C^{q-1}_h \cup \left\{ v_q \right\}, \\ &\text{if } d_{q,h} = \min(\mathbf{d}_q) > d_{max} \Rightarrow C^q_h = C^{q-1}_h,\ C^1_{r+1} = \left\{ v_q \right\}, \end{aligned} \tag{40}$$

meaning that the v_q-th mode is assigned to cluster C_h (which is the closest one in terms of frequency and mode shape) if the similarity value $d_{q,h}$ is smaller than an user-defined threshold d_{max}; otherwise a new cluster C_{r+1} is created containing the v_q-th mode. At the end of the procedure, a certain number nc of clusters defined by their centroids (average value of frequencies, damping ratios, and mode shapes) and cluster sizes (number of poles contained within the clusters) are obtained, and a minimum cluster size can be defined to disregard all those that are not populated enough to be considered as representative samples.

3.4. Damage detection

By applying the automated system identification procedure previously outlined in Section 3.3 to every measurement data, it is possible to obtain the time series of modal features of the structure. Such a process, often called "Frequency tracking", is performed by tracking a reference set of resonant frequencies (typically obtained from an initial AVT) over the dataset of identified modal features. To do so, the poles of every dataset whose frequency values come closest to the reference ones (complying with a user-defined maximum relative tolerance and a minimum MAC value between the corresponding mode shapes) are collected in an observation matrix $\mathbf{Y} \in \mathbb{R}^{n \times N}$, where n is the number of identified frequencies and N is the number of observations. Then, any change in the dynamic behaviour of the structure, possibly related to developing damage, can be detected by the application of statistical process control tools to $\mathbf{Y}$. Nevertheless, as stated earlier in Section 1, environmental/operational factors usually mask the effects of early-stage damage and need to be removed. Therefore, damage detection typically comprises the following two steps: (a) removal of environmental effects, and (b) novelty analysis. Additionally, (c) automated anomaly detection algorithms can be implemented for online damage detection. The implementation of these steps within MOSS is briefly outlined hereafter.

3.4.1. Removal of environmental effects: regression models

Given the masking effects of environmental/operational factors on modal frequencies, the quantities contained in $\mathbf{Y}$ cannot be directly used as damage-sensitive features. Instead, a proper residual error matrix, $\mathbf{E} \in \mathbb{R}^{n \times N}$, is used for this purpose and computed as:

$$\mathbf{E} = \mathbf{Y} - \widehat{\mathbf{Y}}, \tag{41}$$

where $\widehat{\mathbf{Y}}$ contains predictions of the time series of resonant frequencies computed from a baseline in-control population. This in-control population, usually referred to as the *training period*, contains a set of identified modal features that statistically represent the healthy condition of the structure. This must be long enough to cover the full range of environmental conditions (both daily and seasonal fluctuations), and typically a one-year period is assumed adequate. MOSS includes six different regression models to construct $\widehat{\mathbf{Y}}$, three input-output models and three input-only models, namely:

- Input-Output regression models: Multiple Linear Regression (MLR), AutoRegressive with eXogenous input model (ARX), and coupled MLR and Principal Component Analysis (MLR/PCA).
- Input-only regression models: Principal Component Analysis (PCA), Factor Analysis (FA), and Autoassociative Neural Networks (ANN).

In addition, MOSS also includes a Gaussian Mixture Model (GMM) for clustering analysis and detection of freezing conditions. Because of space constraints, the theoretical description of each of these models is omitted in this paper, and interested readers may refer to references [52, 53].

Under the assumption that $\widehat{\mathbf{Y}}$ reproduces the part of the variance of the resonant frequencies corresponding to changes in environmental/operational conditions, $\mathbf{E}$ only contains the residual variance stemming from identification errors and un-modelled environmental/operational effects. If certain damage develops, this only affects the data contained in $\mathbf{Y}$, while $\widehat{\mathbf{Y}}$ remains unaltered. Therefore, $\mathbf{E}$ concentrates the damage-induced variance apt for being used for damage detection purposes.

3.4.2. Novelty analysis

Once the residual error matrix $\mathbf{E}$ is computed, the presence of damage is investigated using control charts as sketched in Fig. 7. These furnish in time a certain statistical distance accounting for disturbances in the distribution of the residuals contained in $\mathbf{E}$. By defining an in-control region, the appearance of out-of-control processes, possibly associated to damage, is detected in the shape of data points violating the in-control region. MOSS includes three different control charts that are overviewed hereafter, namely the Hotelling, Multivariate Cumulative Sum (MCUSUM), and Multivariate Exponentially Weighted Moving Average (MEWMA) control charts. The statistical distances assessed by these control charts are positive by definition, so the in-control region is defined by an interval [0,UCL]. The upper control limit (UCL) is computed as the value of the statistical distance corresponding to a certain confidence level α for the distribution of data within the training population.

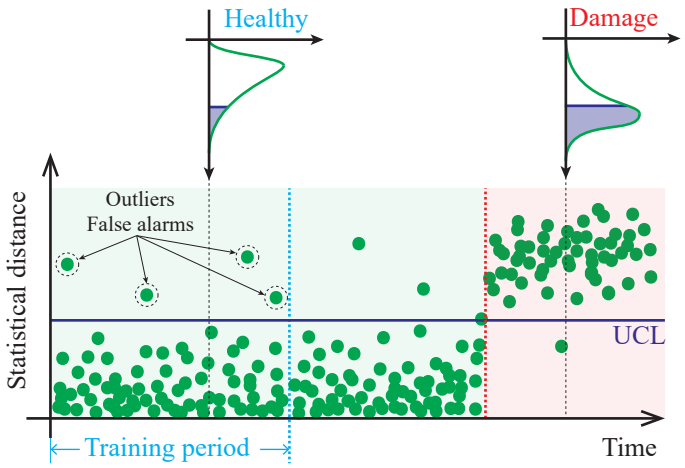

Figure 7: Control chart of a permanent SHM system.

- *Hotelling's* T^2: The Hotelling's T^2 control chart [54] is defined as:

$$T_i^2 = r\left(\overline{\mathbf{E}} - \overline{\overline{\mathbf{E}}}\right)^{\mathrm{T}} \boldsymbol{\Sigma}_0^{-1} \left(\overline{\mathbf{E}} - \overline{\overline{\mathbf{E}}}\right),\ i = 1, 2, \ldots, N/r, \tag{42}$$

where r is an integer parameter referred to as subgroup size, $\overline{\mathbf{E}}$ is the mean of the residuals in the subgroup of the last r observations, while $\overline{\overline{\mathbf{E}}}$ and $\boldsymbol{\Sigma}_0$ are the mean values and the covariance matrix of the residuals statistically estimated in the training period.

- *Multivariate Cumulative Sum (MCUSUM)*: This control chart appears as an improvement of the sensitivity of the T^2 control chart to detect small shifts in the mean of the statistical process, and it is based upon the principle of accumulating information of past observations. Among the different versions of this control chart that can be found in the literature, MOSS includes one of the most commonly used MCUSUM methods proposed by Crosier [55] as:

$$CUSUM_i = \left(r\, \mathbf{S}_i^{\mathrm{T}}\, \boldsymbol{\Sigma}_0^{-1}\, \mathbf{S}_i \right)^{1/2},\ i = 1, 2, \ldots, N/r, \tag{43}$$

with

$$\begin{aligned} C_i &= \left[r \left(\mathbf{S}_{i-1} + \overline{\mathbf{E}} - \overline{\overline{\mathbf{E}}} \right)^{\mathrm{T}} \boldsymbol{\Sigma}_0^{-1} \left(\mathbf{S}_{i-1} + \overline{\mathbf{E}} - \overline{\overline{\mathbf{E}}} \right) \right]^{1/2}, \\ \mathbf{S}_0 &= \mathbf{0}, \\ \mathbf{S}_i &= \begin{cases} \mathbf{0}, & \text{if} \quad C_i \leq k, \\ \left(\mathbf{S}_{i-1} + \overline{\mathbf{E}} - \overline{\overline{\mathbf{E}}} \right)(1 - k/C_i), & \text{if} \quad C_i > k, \end{cases} \end{aligned} \tag{44}$$

where k is a constant parameter. Specific expressions for setting k can be found in reference [55]. MOSS imposes a default value of $k = 0.5$.

- *Multivariate Exponentially Weighted Moving Average (MEWMA)*: Originally proposed by Lowry *et al*. [56], the MEWMA control chart represents an intermediate solution between the T^2 and the MCUSUM control charts. Alike the MCUSUM control chart, the MEWMA method also accounts for the information from past observations, although it gives weights decreasing in a geometric progression from the most recent observation to the first one. The statistical distance used in the MEWMA control chart reads:

$$MEWMA_i = \left(r\, \mathbf{z}_i^{\mathrm{T}} \boldsymbol{\Sigma}_{z_i}^{-1} \mathbf{z}_i \right)^{1/2},\ i = 1, 2, \ldots, N/r, \tag{45}$$

with

$$\begin{aligned} \mathbf{z}_i &= \lambda \left(\overline{\mathbf{E}} - \overline{\overline{\mathbf{E}}} \right) + (1 - \lambda) \mathbf{z}_{i-1}, \\ \boldsymbol{\Sigma}_{z_i} &= \lambda \frac{1 - (1 - \lambda)^{2i}}{2 - \lambda} \boldsymbol{\Sigma}_0, \end{aligned} \tag{46}$$

where λ is a smoothing constant with $0 \leq \lambda \leq 1$. Practically, the most often used value of λ is 0.1.

3.4.3. Automated damage detection

An alarm system based upon the detection of outliers in the control chart would result in an excessive number of false alarms. Note that the control limit UCL is defined for a certain confidence level α, so such a system would signal a proportion of $1 - \alpha$ alerts even when the structure remains in healthy condition (see Fig. 7). Therefore, it is necessary to implement a detection algorithm based upon variations in the statistical distribution of statistical distances. To do so, MOSS implements a simple but efficient approach based upon the pruned exact linear time (PELT) method proposed by Killick and co-authors [57]. This algorithm searches for a change-point or time instant at which some statistical property of a signal changes abruptly. In particular, we focus on the detection of mean shifts in the time series of residuals in $\mathbf{E}$. Considering a certain row of the error residual matrix $\mathbf{E}$ as a signal $x_1, x_2, ..., x_N$, the algorithm finds a position cp in a time series that minimizes the following cost function:

$$J = \sum_{i=1}^{cp-1} \left(x_i - \frac{1}{cp-1} \sum_{r=1}^{cp-1} x_r \right)^2 + \sum_{i=cp}^{N} \left(x_i - \frac{1}{N - cp + 1} \sum_{r=cp}^{N} x_r, \right)^2 \tag{47}$$

To do so, the PELT algorithm iteratively segments the time series until finding the optimal solution. Through the use of dynamic programming and pruning, it can be proved that the computational cost of the PELT method is linear in the number of data points. For more specific information about the implementation of the PELT method, readers may refer to reference [57].

In this light, an automatic damage detection algorithm is implemented in MOSS based upon the PELT method. This is automatically launched every time the code finds a new data file and computes a new column of $\mathbf{E}$. The position of the change-points detected by the PELT method is arranged in a matrix $\mathbf{P} \in \mathbb{R}^{n \times N}$, and the number of repetitions (i.e. number of consecutive times that the PELT algorithm finds the same change-point) are collected in a vector $\mathbf{N} \in \mathbb{R}^{n}$. When a change-point is detected within the training period t_p, a zero value is assigned to the corresponding position in $\mathbf{P}$. The algorithm stops and signals an alarm when any of the elements of $\mathbf{N}$ reaches an user-defined maximum number of repetitions cp_{max}. For clarity, the algorithm is illustrated in the following pseudo-code:

Algorithm 1 Pseudo-code for online damage detection using the PELT method.

for $i \leftarrow 1, n$ **do**
    PELT method $\leftarrow cp_i$
    if $cp_i \leq t_p$ **then**
        $\mathbf{P}_{N+1,i} = 0$
    else
        $\mathbf{P}_{N+1,i} = cp_i$
    if $\mathbf{P}_{N+1,i} = \mathbf{P}_{N,i}$ **then**
        $\mathbf{N}_i = \mathbf{N}_i + 1$
    else
        $\mathbf{N}_i = 0$
if $\max(\mathbf{N}) = cp_{max}$ **then**
    Signal alarm

4. MOVA/MOSS description and application case study

The overarching purpose of MOSS is the fully autonomous management of permanent integrated SHM systems. Typically, the work-flow of an SHM system using MOSS is sketched in Fig. 8. The monitoring system consists of an integrated sensor network deployed on the structure of interest, and of an in-place DAQ system that permanently collects the monitoring data. Subsequently, computer files containing monitoring records of certain time duration are sent through the internet or another data transmission system to a server or to the cloud where the data are stored. Here MOSS automatically processes all the monitoring records and updates user-defined control charts. To do so, it distinguishes between dynamic measurements and measurement data of different nature (e.g. temperature sensors, strain gauges, or inclinometers). On one hand, MOSS performs automated OMA using the ambient vibration records according to the methodology previously introduced in Section 3.3. This process comprises five sequential steps, namely (i) pre-processing of measurement records according to certain user-defined filtering process; (ii) automated OMA; (iii) frequency tracking; (iv) elimination of environmental effects through pattern recognition techniques; and (v) control charts and online anomaly detection. In parallel, MOSS processes the rest of measurement data and performs data fusion. Specifically, the user can freely decide to use these extra monitoring data as predictors and/or estimators. That is to say, non-dynamic monitoring data can be used to filter out the environmental effects over the resonant frequencies or, alternatively, they can be used as damage-sensitive features. In the latter case, anomalies in their time series are investigated likewise vibration data through control charts. Therefore, MOSS permits the definition of multiple control charts and performs simultaneous online damage detection of diverse damage-sensitive features.

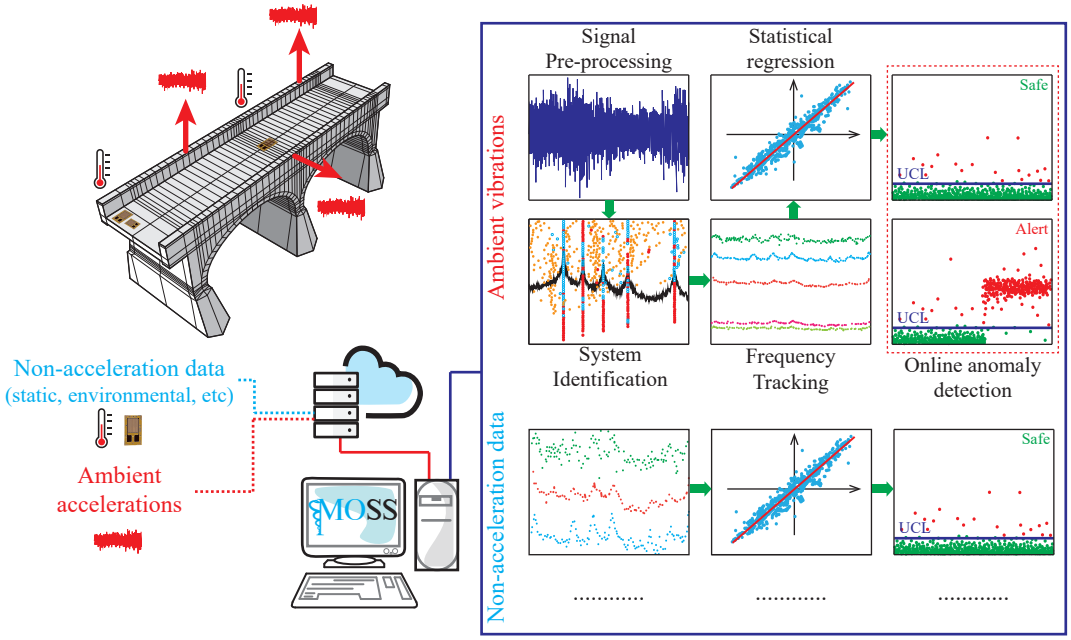

Figure 8: Schematic of a permanent SHM system using MOSS.

The main GUI of MOSS is shown in Fig. 9. The interface is organized in four consecutive steps:

I **System Identification**: This step encompasses the main capabilities of MOVA for AVT, and has the purpose of defining the geometry of the structure and the signal processing procedure used for all the measurement records. This includes the following sub-sections: *GEOMETRY*, *SIGNAL PRE-PROCESSING*, *SYSTEM IDENTIFICATION*, and *Extra monitoring variables*. The latter allows the user to introduce as many non-dynamic sensors as desired by providing a reference label, the measurement unit, and the computer folder that contains the record files.

II **Process of initial data set**: This step includes the sub-section named *Process initial data set* and generates an initial data population of modal features to be used in the subsequent steps. The initial dataset of measurements (preferably those corresponding to the training period) along with the results folders (including the processed signals and the identification results) are introduced through the file manager located in the left part of the interface.

III **Frequency tracking and elimination of environmental effects**: This comprises the sub-sections named *FREQUENCY TRACKING* and *MULTIVARIATE STAT. ANAL. (MSA)*, and it is devoted to defining the parameters for automated frequency tracking and the statistical models used for pattern recognition. Additionally, an extra module (*SURROGATE MODEL*) for damage identification (i.e. detection, localization, and quantification) by means of surrogate-based model updating is anticipated for future releases.

IV **Damage detection**: This last step constitutes the core of MOSS, and performs the online damage detection of the previously defined damage-sensitive features. It includes the sub-sections indicated as *Continuous SHM* and *Damage simulation*. The latter allows the user to explore the effects of artificial damage upon the constructed control models.

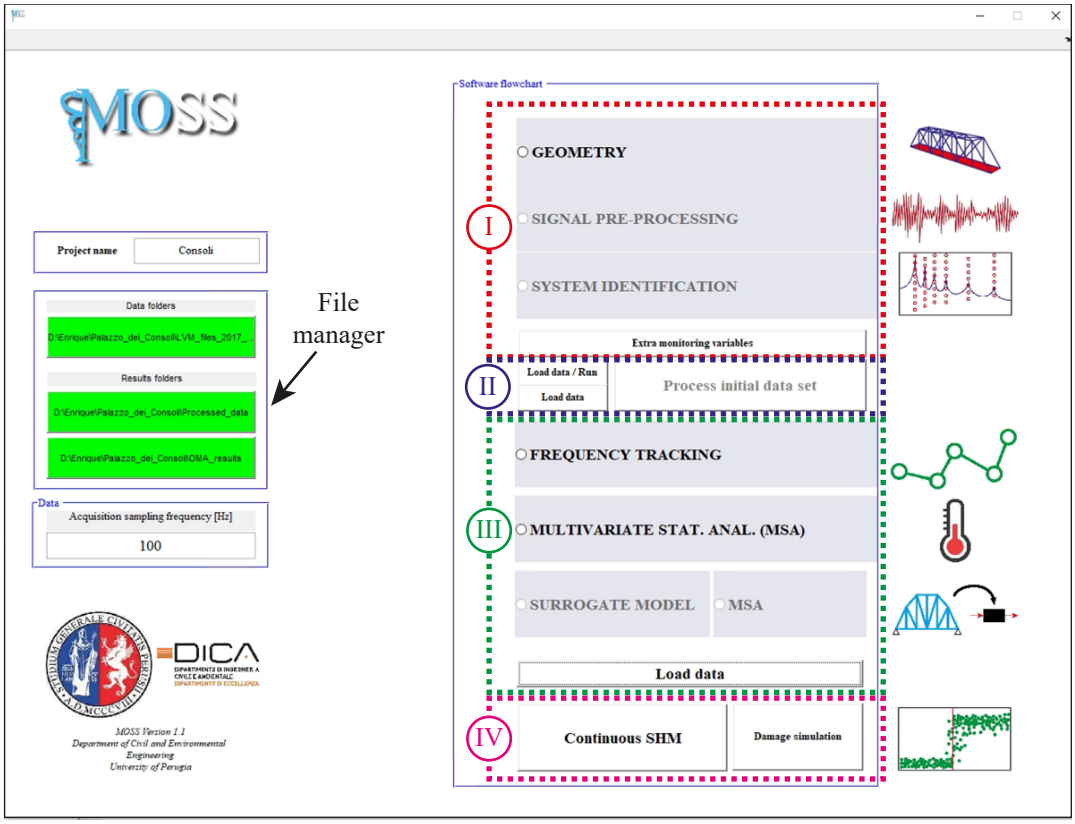

Figure 9: MOSS main GUI.

Geometry module: This interface allows the definition of a geometrical model and the accelerometer layout for the representation of the mode shapes. Three-dimensional models can be constructed using nodes, lines, and planes, as well as kinematic conditions between active and slave nodes. Every active node is defined at least by a measurement channel and the corresponding direction/orientation ($\pm x$, $\pm y$, or $\pm z$). Kinematic conditions include rigid-plane diaphragms and link conditions between slave and active nodes. Additionally, the interface incorporates a formula editor allowing for inserting general symbolic constraints between sets of nodes. The whole process can be carried out graphically using the mouse, manually by typing the information directly in the edit tables, or by loading a geometry file in ASCII format. Figure 10 (a) shows the geometrical model built for the AVT of the Consoli Palace previously described in Fig. 1. The model includes 9 acceleration channels and rigid-plane diaphragms at each floor of the building. For illustrative purposes, Fig. 10 (b) shows two sample geometries defined for a bridge structure and a tower.

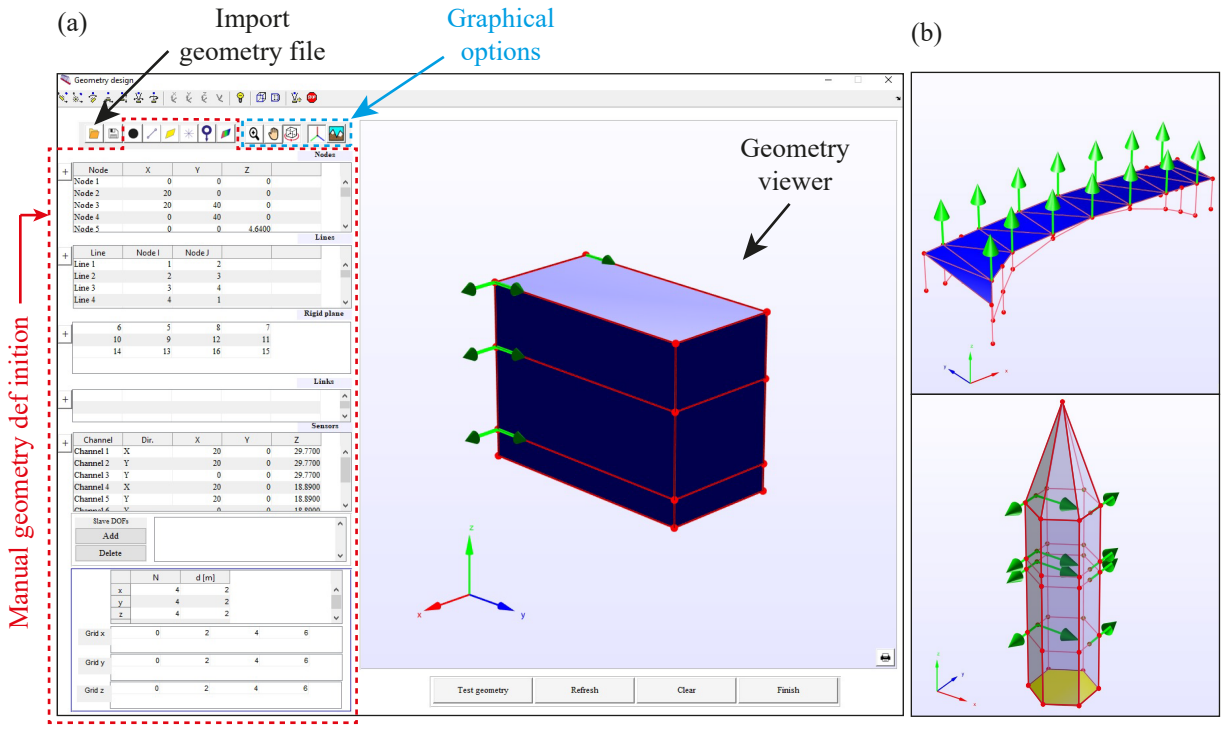

Figure 10: Screenshot of the geometry module: (a) Consoli Palace, (b) reinforced-concrete bridge and masonry tower.

Signal pre-processing module: This module, shown in Fig. 11 (a), permits the definition of signal processing sequences to minimize the effects of noise and the presence of abnormal events. Specifically, the software interface includes: signal downsampling, moving average filtering, linear detrend, band-pass filtering, Hanning window filtering of signal spikes, Hanning window filtering of non-stationary excitations produced by swinging bells (common in CH structures), and a robust Multichannel Singular Spectrum Analysis (MSSA) denoising approach [58]. The software accounts for the application order of the selected filtering techniques, and the graphical representation of the filtered signals against the raw ones enables users to check the effectiveness of the implemented signal processing sequence. The comparison can be performed in the time domain, through PSDs, time-frequency analysis, and SVs of the PSDs (see Fig. 11 (b)). Specifically, Fig. 11 presents the pre-processing of the accelerations recorded during the AVT of the Consoli Palace conducted on May 4th 2017. In this case, ambient vibration data were collected during 30 min at a sampling frequency of 1652 Hz. The raw signals evidence the strong effect of the swinging bells located in the bell-tower of the palace, which ring regularly every 15 minutes. In order to minimize these effects and improve the system identification, the selected signal processing sequence includes: downsampling to 40 Hz, linear de-trend, moving average filtering with time window length of 200 s, and Hanning window filtering to eliminate the effect of swinging bells and signal spikes. Note that the swinging of bells induces a significant violation of the white noise assumption and must be filtered out before conducting the system identification. The implemented time-domain Hanning window filter suppress those parts of the signals affected by swinging bells, in such a way that the resulting signals do comply with the white noise assumptions.

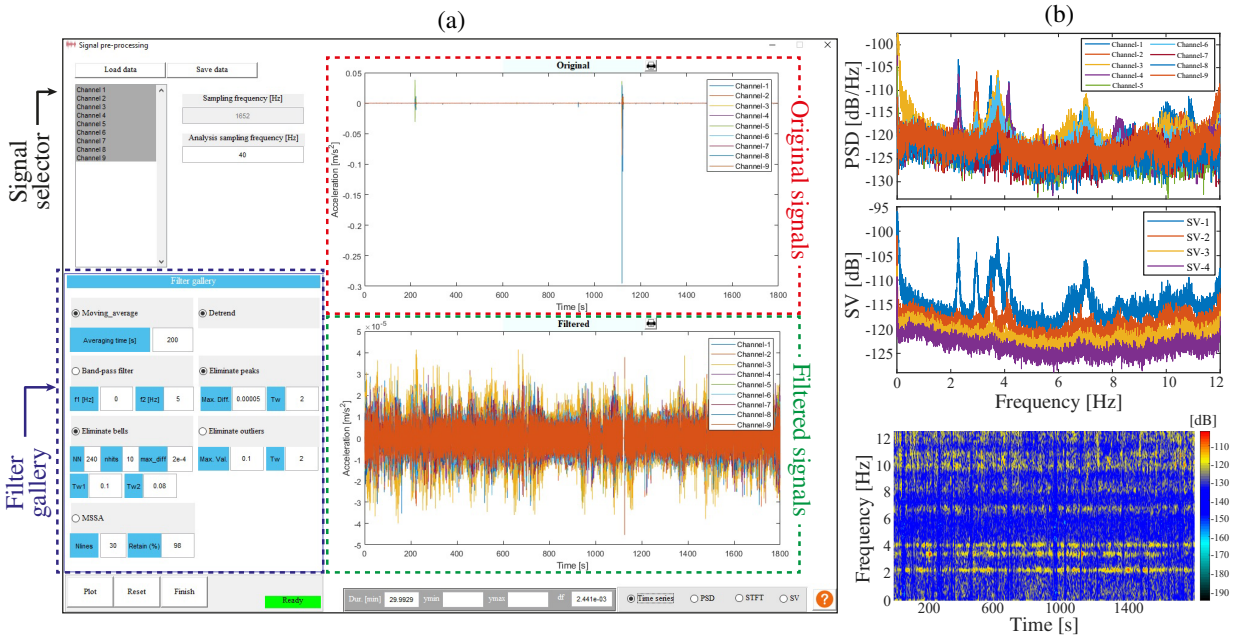

Figure 11: Screenshot of the signal pre-processing module (a), and analyses of the filtered signals (b).

System identification module: This interface manages the vibration-based identification of the structure. Here the user can select any of the identification techniques previously introduced in Section 3. The identification results are presented in the shape of tabulated data, stabilization diagrams (SSI and p-LSCF), or SVs of the PSDs (EFDD), exportable reports, and the histogram representation of the MAC matrix. Moreover, this interface counts on a specific section for mode shape representation, including the animation of complex modes, complexity plots, and display of quality factors such as the Mode Complexity Factor (MCF), Mode Phase Collinearity (MPC), and Mean Phase Deviation (MPD). As an example, Fig. 12 (a) shows a screenshot of this module with the identification results obtained with the AVT of the Consoli Palace using COV-SSI, and Fig. 12 (b) shows a screenshot of the mode shape representation interface with the analysis of the first vibration mode.

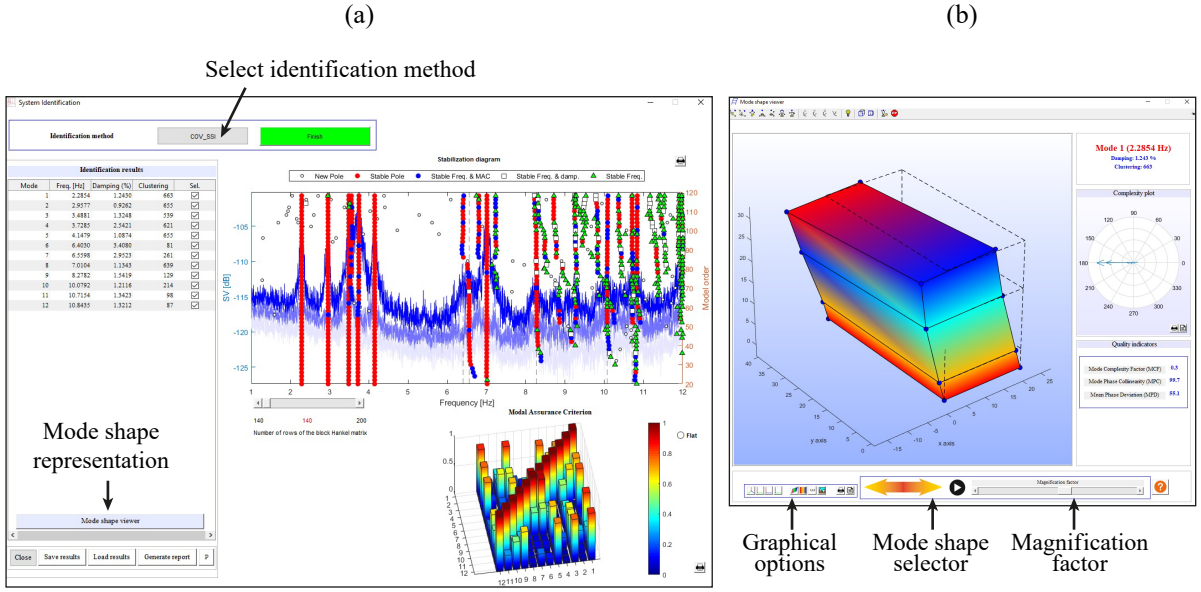

Figure 12: Screenshots of the system identification module (a) and mode shape viewer (b).

This module has been utilised for the system identification of the Consoli Palace using the ambient acceleration data collected during the AVT and formerly processed in the signal pre-processing module. The identification results using all the available methods in MOSS are presented in Table 1. As reported earlier, six clear modes

are identified in the frequency range from 0 to 12 Hz. These correspond to two global first bending modes in the $x-$ and $y-$directions, denoted as Fx1 and Fy1, respectively, one global torsional mode, T1, and three local modes related to the interaction between the palace and the bell-tower, denoted as L1, L2, and L3. The global mode shapes obtained using COV-SSI in MOSS are depicted in Fig. 13. It is noted that very similar resonant frequency estimates are obtained by all the different identification methods, while large differences are found in terms of damping ratios. The quality of damping estimates is highly dependent on the level of excitation of the structure, which is often quite low in CH structures in operational conditions. This is specially critical in this case study, where ambient accelerations in the palace did not exceed 1.5E-3 m/s^2, so substantial uncertainties are expected to arise in the determination of damping properties.

Table 1: Vibration-based system identification results of the Consoli Palace through the AVT conducted on May 4th 2017 using the EFDD, p-LSCF, COV-SSI, and DATA-SSI methods in MOSS.

	Natural frequencies [Hz]				Damping ratios [%]			
Mode	EFDD	p-LSCF	COV-SSI	DATA-SSI	EFDD	p-LSCF	COV-SSI	DATA-SSI
Fx1	2.270	2.296	2.285	2.287	1.471	0.561	1.243	1.383
Fy1	2.953	2.970	2.958	2.961	0.361	0.166	0.926	1.017
L1	3.479	3.463	3.488	3.492	0.247	0.118	1.325	1.387
L2	3.740	3.723	3.729	3.717	0.352	1.767	2.542	2.824
T1	4.153	4.124	4.148	4.150	0.303	0.423	1.087	1.226
L3	6.986	7.016	7.010	7.008	0.138	0.549	1.134	1.121

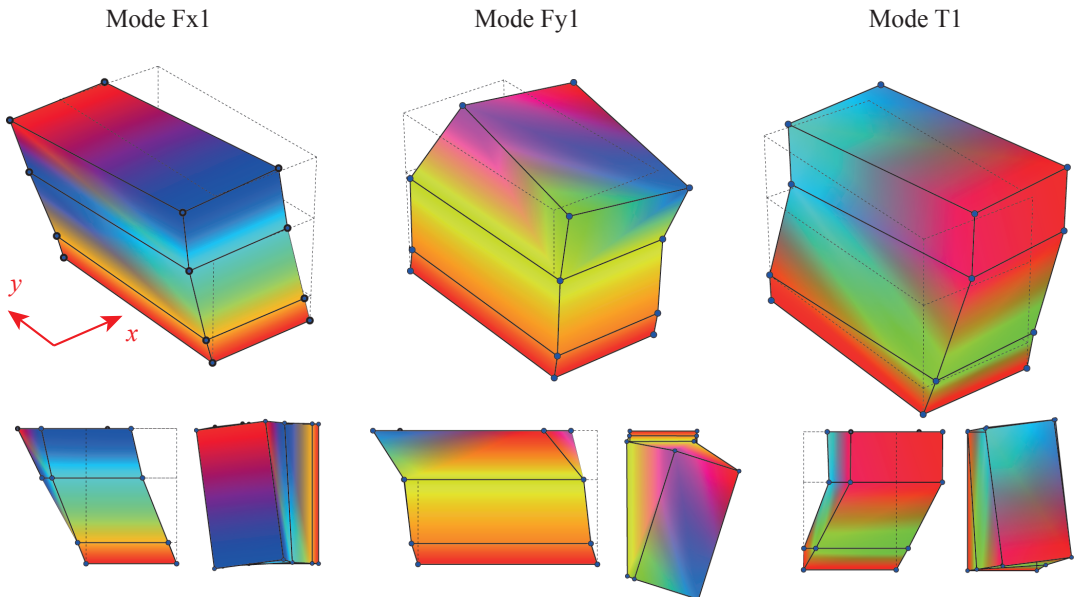

Figure 13: Global mode shapes, first bending modes Fx1 and Fy1 and torsional mode T1, obtained from the AVT of the Consoli Palace using COV-SSI.

Frequency tracking module: Once the initial data population has been processed, this module allows to extract the time series of resonant frequencies, damping ratios, and mode shapes of the structure. To do so, the user must introduce a reference set of frequencies (typically retrieved from an AVT using a relatively large set of sensors) and a set of tolerances on allowable maximum relative frequency variations and minimum MAC values. Figure 14 shows a screenshot of this interface with the results obtained from the long-term monitoring of the Consoli Palace. The vibration-based identification of the palace was conducted using COV-SSI according to the automation procedure previously presented in Section 3.3. In this case, only five modes corresponding to Fx1, Fy1, L1, T1, and L3 were tracked, while Mode L2 was disregarded because of difficulties in its separation from modes L1 and T1. This is due to the reduced number of sensors used in the monitoring (only 3), what hinders the discrimination of very closely spaced modes by means of MAC comparison. Special attention must be also devoted to the potential occurrence of freezing conditions. Typically, freezing air temperatures induce the formation of ice crystals in the micro porosity of mortar joints in masonry structures leading to an overall

stiffening effect and, as a result, the natural frequencies experience substantial increases [18, 59]. Specifically, freezing conditions are clearly visible in the time series of the resonant frequencies of the Consoli Palace in Fig. 14 during the time period from February 25th to March 1st 2017. In order to automatically detect such conditions, the frequency tracking interface counts on a specific section for that purpose. This section incorporates a gradient-based detection algorithm that allows to identify data regions of certain time length (336 h in the example of Fig. 14 and marked with black dashed lines) with sudden increases in the resonant frequencies. Once detected, the user can introduce new tolerance values for performing local frequency tracking over these regions. Afterwards, freezing conditions can be tackled in two different ways: using clustering analysis and setting different statistical regression techniques as illustrated later, or directly dismissing the identification results corresponding to the detected regions. The latter approach is acceptable when freezing conditions only occur during short periods of time.

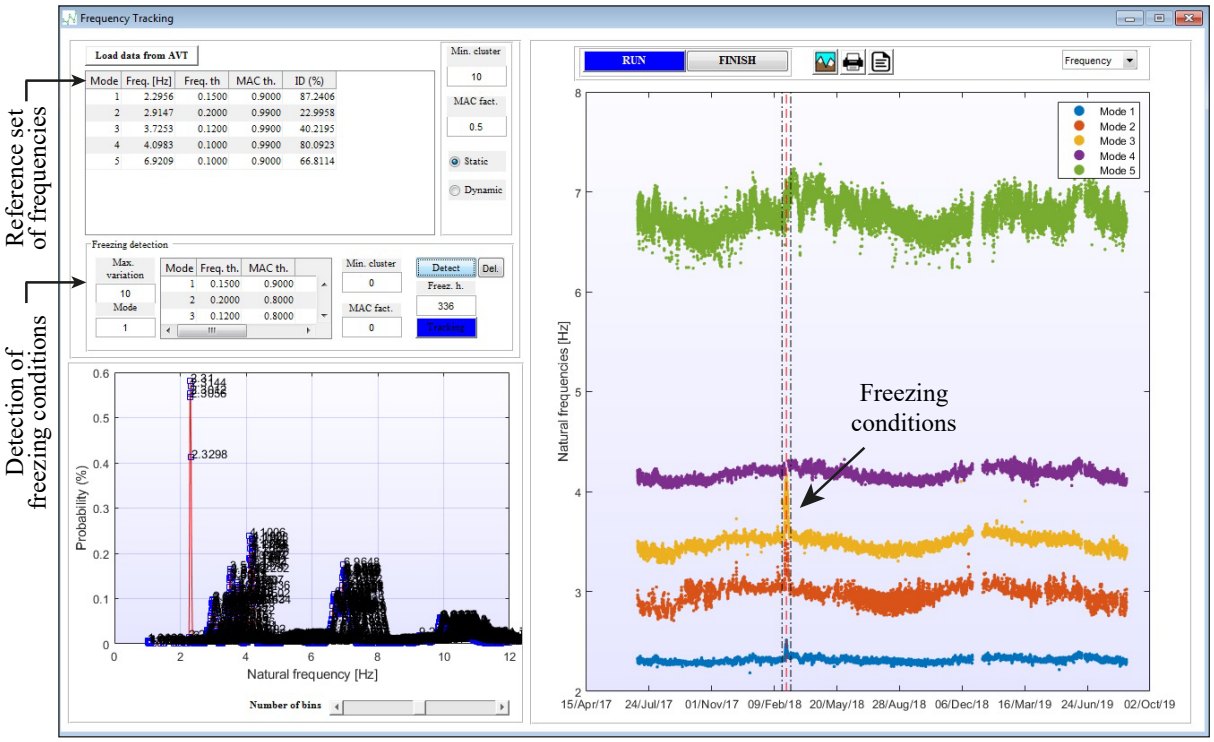

Figure 14: Screenshot of the frequency tracking module with identification results of the permanent SHM system installed in the Consoli Palace.

Multivariate statistical analysis module: This module, shown in Fig. 15, permits the definition of different statistical models accounting for distinct damage-sensitive features. Every model, identified by an user-defined label name, is assessed through statistical pattern recognition in the subsequent damage identification module. Specifically, this interface includes the following features:

- **Outliers elimination**: Outliers represent anomalous data points arising as a result of identification and/or tracking errors. Their presence in the time series of damage-sensitive features may drastically reduce the effectiveness of regression models for the elimination of environmental effects, and it can grossly distort the computation of the mean and covariance matrices used later for statistical process control. With the aim of reducing the number of outliers in the training period (when the structure is assumed to be in the healthy state), this interface includes the PCA-based methodology for outliers elimination proposed by Wah *et al*. [60].

- **Filling of missing data**: A very common situation in vibration-based SHM concerns the incomplete identification of the dynamic features in the frequency range of interest. This may be due to tracking errors or to low or anomalous excitation conditions precluding the identification algorithm to find some of the modes of vibration. This results into missing data in the observation matrix. To solve this issue, this module includes three different filling methods: linear interpolation, autoregressive modelling, and a PCA-based algorithm for filling data gaps.

- **Clustering analysis**: The interface incorporates a GMM for detection of freezing conditions. In particular, the algorithm classifies the damage-sensitive features into two separate groups of dissimilar variance. Then, different regression methods can be built for each data cluster and so remove the environmental effects in a more effective manner.

- **Estimators/Predictors definition**: Every statistical model is defined by a set of estimators (independent variables) and predictors (dependent variables). The user can freely select as estimators and/or predictors the resonant frequencies, damping ratios, max/min acceleration values, and acceleration root-mean-squares (RMS), as well as the mean, max/min, and standard deviation values of the non-dynamic measurements. Additionally, the interface incorporates a *variable calculator* that allows to define new estimators/predictors by typing general mathematical expressions involving different variables. This includes the possibility of adding time delays in certain parameters to build dynamic regression models, that is to say, models accounting for past observations of certain predictors to account for thermal capacitance effects (e.g. the dynamics of heating up and cooling down processes).

- **Build of statistical models**: The user can select among six different regression models, including output-only (PCA, FA, and AANN) and input-only models (MLR, ARX, and MLR/PCA).

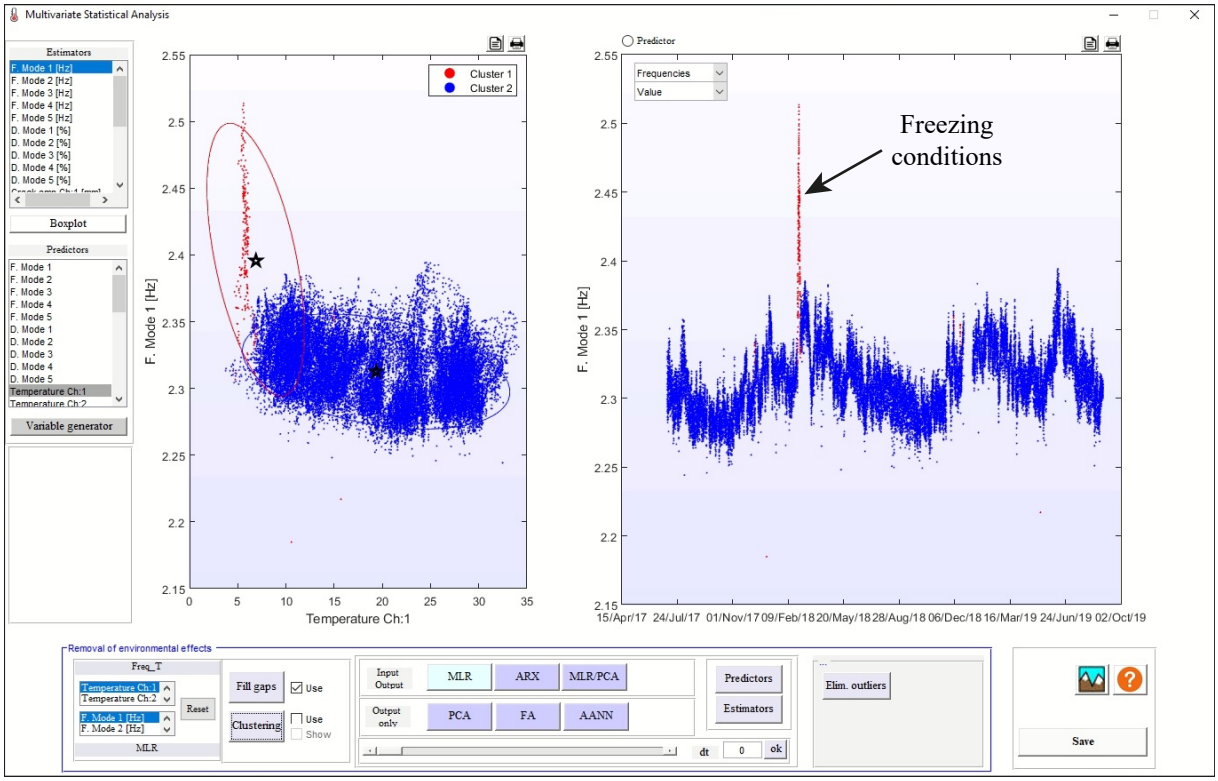

Figure 15: Screenshot of the multivariate statistical analysis module with the clustering results of the resonant frequencies of the Consoli Palace identified during the first year of monitoring.

The results in Fig. 15 show the application of GMM clustering for identification of freezing conditions in the case study of the Consoli Palace. It is noted that the sudden increase of natural frequencies induced by freezing conditions can be accurately detected by the model. Then, different statistical models can be applied to eliminate the environmental effects in each of the identified clusters. Nevertheless, for the sake of simplicity, and given that freezing conditions were only observed once during the whole monitoring period, the dataset corresponding to freezing conditions have been dismissed when using the *frequency tracking* module. On this basis, Fig. 16 analyses the correlation between the mean temperature and crack amplitudes assessed by LVDT-1 (C1) against the resonant frequencies of global modes Fx1, Fy1, and T1 of the Consoli Palace during the one-year training period. In this figure, it is noted that the resonant frequencies exhibit a negative correlation with the mean temperature, and vice versa for the crack amplitudes. The negative frequency/temperature correlation can be conceivably ascribed to temperature-induced softening of metallic tie rods installed in the interior of the building. This agrees with previously reported results in the literature, such as the work by Gentile and co-authors [33] who identified the

role of metallic tie rods in the development of negative frequency/temperature correlations in the Milan Cathedral. On the other hand, the positive frequency/crack amplitude correlation is explained by the correlation between temperature and crack amplitudes. In particular, temperature increases induce the closure of cracks and vice-versa for temperature decreases. For a more exhaustive analysis of the environmental effects on the Consoli Palace, readers may refer to reference [22].

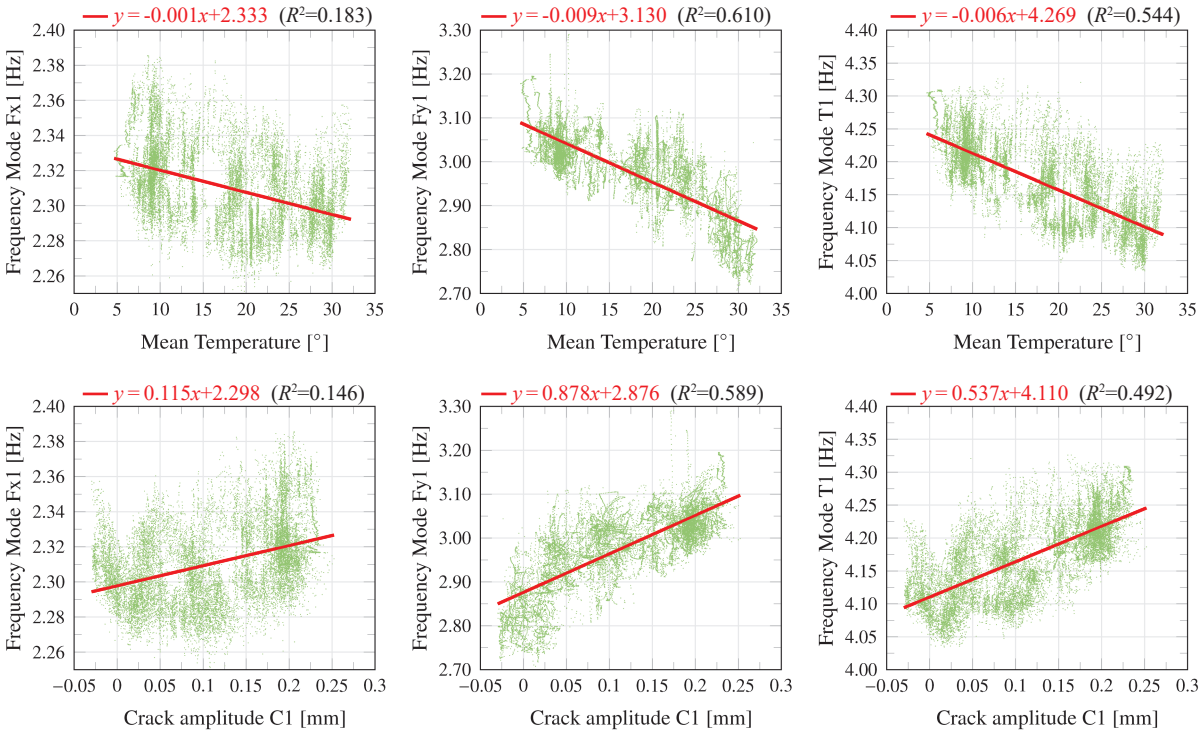

Figure 16: Correlation between mean temperature and crack amplitudes assessed by LDVT-1 and the resonant frequencies of global modes Fx1, Fy1, and T1 of the Consoli Palace during the one-year training period.

In light of the previous analyses, three different statistical models are defined in the *Multivariate statistical analysis* module, labelled as MLR-F, PCA-F and ARX-C. Models MLR-F and PCA-F define the resonant frequencies as estimators, while ARX-C considers for this purpose the crack amplitude C1. The aim of these models is to perform a local/global damage assessment of the Consoli Palace. On one hand, the first two models evaluate the presence of damage affecting the overall stiffness of the structure, while the second one accounts for local damage inducing behavioural variations in the amplitudes of crack C1. In the PCA-F model, only two principal components (PCs) sufficed to explain more than 90% of the variance of the estimators. The characteristics of these statistical models are as follows:

- MLR-F: Estimators → {Fx1, Fy1, L1, T1, L3}; Predictors → {T1, T2, C1, C2}; Regression model → MLR.
- PCA-F: Estimators → {Fx1, Fy1, L1, T1, L3}; Regression model → PCA (retained PCs: 2).
- ARX-C: Estimators → {C1}; Predictors → {T1, T2}; Regression model → ARX.

Figure 17 depicts the statistical predictions obtained for all the defined models and the corresponding Hotelling's T-square control charts. For clarity purposes, only the time series of the frequencies of mode Fx1 and crack amplitudes C1 are plotted in the figure during the one-year training period. With regard to the statistical predictions obtained by models MLR-F and PCA-F, it is noted that better fittings of the natural frequency of Fx1 are obtained using PCA. Conversely, larger differences between experimental and statistical predictions are observed in the MLR-F model. In this case, it is noted that although the use of temperature and crack amplitude measurements allows the modelling of the daily and, to some extent, seasonal variations in the resonant frequencies, there are still some seasonal fluctuations that cannot be accurately reproduced. This may be ascribed to the specific sensor locations, which may fail at characterising the temperature distribution throughout the building. On the other hand, it is noted in the ARX-C model that the use of temperature measurements as exogenous variables can well reproduce both the seasonal and daily fluctuations in the time series of crack amplitudes C1. However, it is important to remark that the statistical predictions using a MLR model instead of an autoregressive model led to

large residuals. Specifically, while seasonal fluctuations could be captured sufficiently well using only temperature measurements as predictors, daily fluctuations could be not accurately reproduced. This fact may indicate the correlation of crack amplitudes with the temperature distribution in different locations of the building (recall that the temperature sensors are located right aside the LVDTs). The graphs in the right hand side of Fig. 17 reports the time series of T^2 distances along with the UCL corresponding to a confidence level of 99%. Here, it is noted that the number of outliers after the training period is slightly larger in the MLR-F model (6.03%) compared to the PCA-F (2.85%), which confirms the better fitting of the experimental data using PCA.

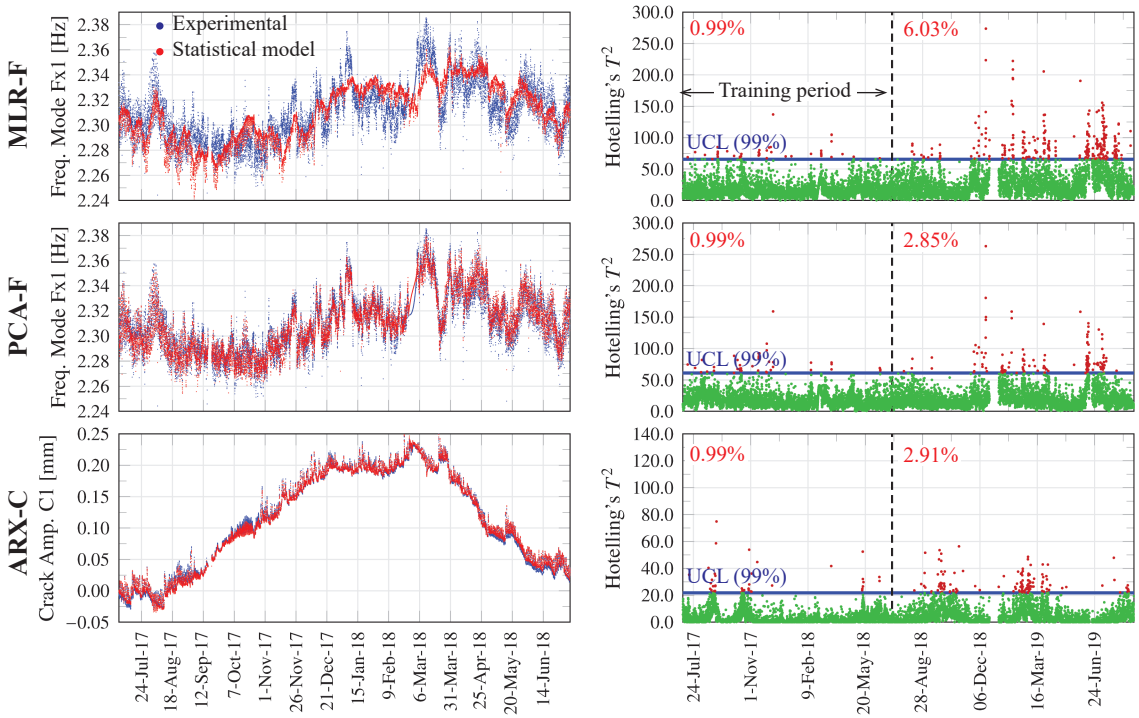

Figure 17: Plots of time histories of the natural frequency of mode Fx1 and crack amplitude C1 obtained by statistical models MLR-F, PCA-F, and ARX-C, and corresponding Hotelling's T-square control charts.

Damage detection and simulation modules: The damage detection module, shown in Fig. 18, allows to manage permanent SHM systems in real-time and in a completely autonomous way. The interface includes real-time graphs of the time series of the estimators, predictors, and measurement data, as well as the corresponding control charts. Every time a new data file is found, the interface graphs are updated and the software performs damage detection based on all the previously defined statistical models. If an anomaly is found in any of the models, the software triggers an alert and notifies the user with a sound-alert, an alert message in the console of the interface, and (if desired) an e-mail with an attached screenshot of the control chart with the detected anomaly. In this way, the user can check whether a system notification may be a false alarm or, conversely, an in-situ inspection ought to be planned. The work-flow of this interface comprises the following steps: (a) automatic detection of new data files, signal pre-processing, system identification, and frequency tracking; (b) construction of statistical models, elimination of environmental effects, and updating of control charts; and (c) automatic damage detection. The progress of each step is notified in the console of the interface. Moreover, if no files are found in a maximum period of time prescribed by the user, the software sends a warning notification of unintended system shutdown.

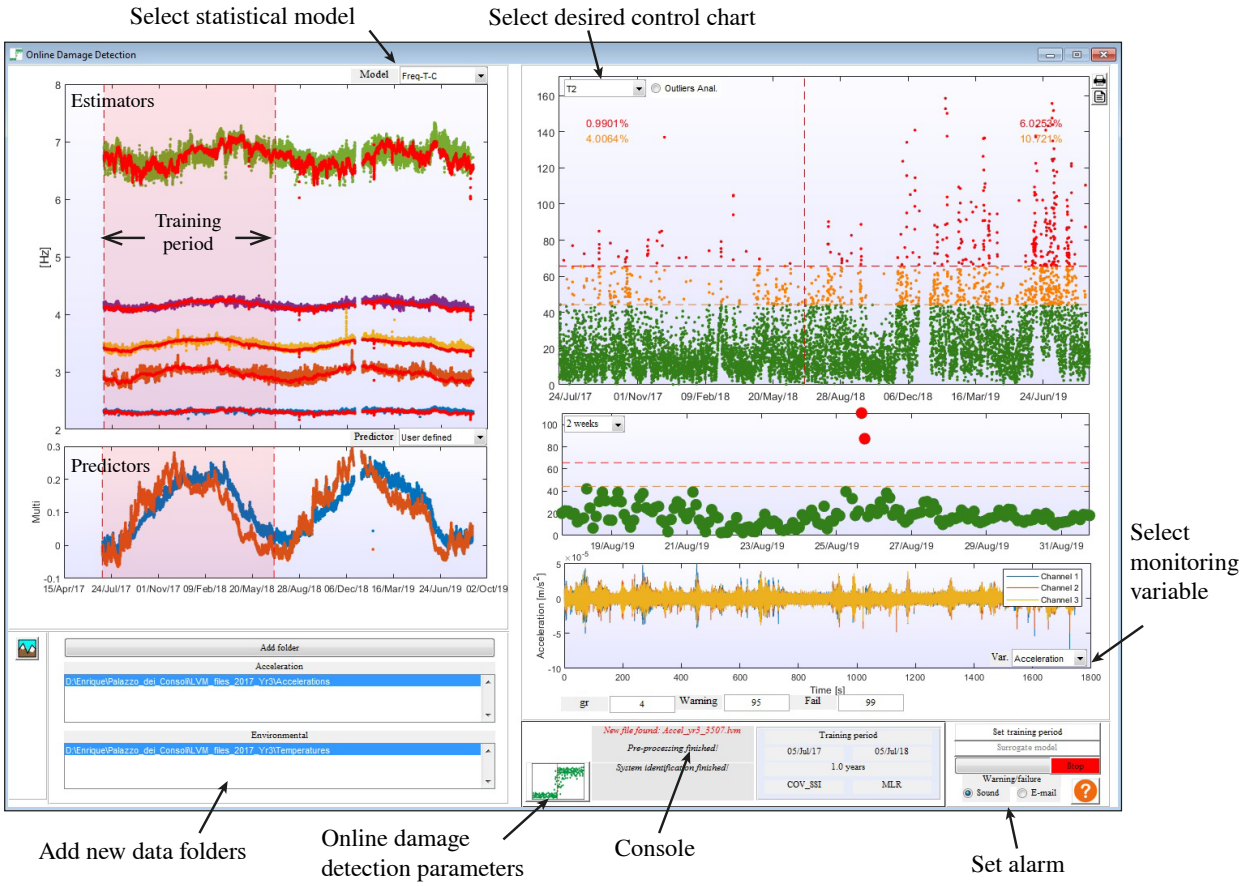

Figure 18: Screenshot of the damage identification module.

Note that a damage detection algorithm based upon the detection of outliers in the control charts would lead to a large number of false alarms. In particular, considering a subgroup size of 4 and a UPC of 99%, this would result in $(365 \cdot 24 \cdot 2/4)/100 = 43.8$ alarm notifications per year on average, even when the structure remains in healthy conditions. To minimize the rate of false alarms, MOSS includes the newly proposed damage detection method in Section 3.4.3. Moreover, in order to tune the convergence parameter cp_{max} and assess the effectiveness of a statistical model for damage detection, the software also counts on a *Damage Simulator* module available in the last section of the main GUI in Fig. 9. This allows the user to introduce artificial damage scenarios in terms of mean shifts in the estimators from a given date forward. As an example, Fig. 19 shows the control charts obtained for the previously defined statistical models (MLR-F, PCA-F, and ARX-C) when artificial damage is introduced from August 20st 2018. In particular, frequency decays of $\Delta f_1 = -3.44$E-2 Hz ($-1.5\%\overline{\text{Fx1}}$) and $\Delta f_1 = -2.53$E-2 Hz ($-1.0\%\overline{\text{Fx1}}$) are introduced in the time series of the resonant frequency of mode Fx1 for MLR-F and PCA-F models, respectively. It is important to remark that, given the inferior fitting performance of the MLR-F model formerly reported in Fig. 17, a larger frequency decay value was necessary in this case to successfully detect the imposed damage. In the case of the ARX-C model, a mean shift of 1.10E-2 mm ($10\%\overline{\text{C1}}$) is included in the time series of crack amplitudes C1. A convergence parameter value of $cp_{max} = 96$ is assumed, that is to say, the same anomaly must be detected in 96 consecutive steps (48 hours since every file is 30-min long) to be considered as a potential fault.

Note that in Fig. 19 the imposed damage scenarios were successfully detected by all the statistical models. Additionally, a total of 15, 17, and 14 false positives are detected for the MLR-F, PCA-F, and ARX-C models, respectively. These are indeed related to noticeable shifts in the corresponding residuals and arise even when no damage is introduced. This circumstance evidences limitations of the statistical models to reproduce certain in-control operational and/or environmental effects. It is thus concluded that the fitting efficiency of the selected statistical models within the training period determines the minimum detectable damage and the appearance rate of false alarms. In the particular case of the Consoli Palace, a denser monitoring of the temperature distribution in the building, as well as of other environmental factors such as the humidity in the masonry, may reduce the minimum detectable anomalies and the false alarm rate.

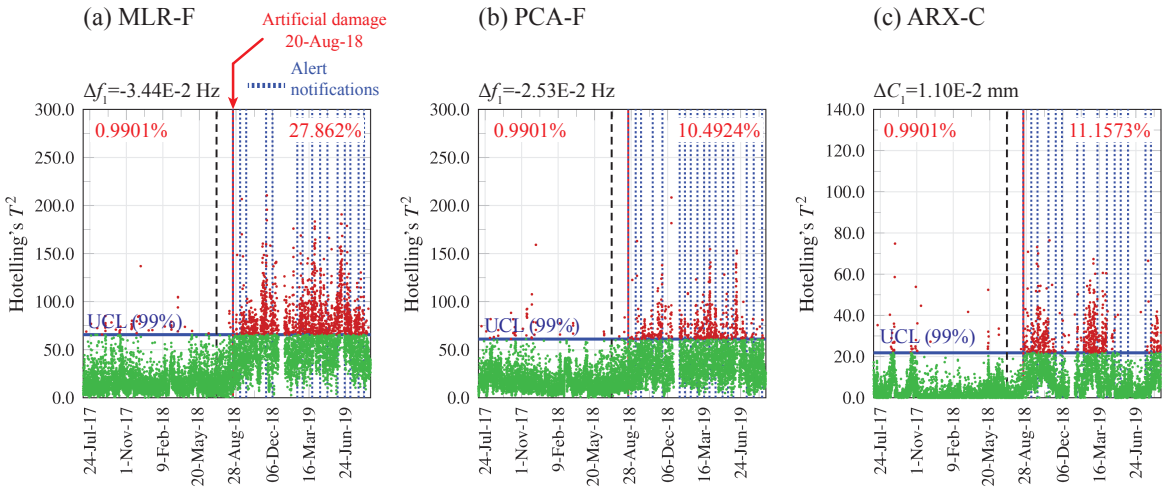

Figure 19: Automatic detection of simulated damage scenarios applied to the monitoring time series of the Consoli Palace considering different statistical models: (a) MLR-F, (b) PCA-F, and (c) ARX-C.

5. Concluding remarks

This paper has presented the development of two novel software solutions, MOVA and MOSS, for the automatic management of permanent integrated SHM systems. The developed software includes intuitive GUIs to guide users all through the process until the setting of a completely autonomous SHM system. The code comprises a unique collection of state-of-the-art algorithms and tools for vibration-based SHM, and allows the fusion of heterogeneous monitoring data for comprehensive structural assessment. In addition, a novel anomaly detection algorithm based upon the PELT method has been implemented for performing automatic damage detection. The capabilities of MOVA/MOSS have been demonstrated through a real case study of a CH structure, the Consoli Palace in Gubbio (Italy). A mixed static/dynamic monitoring system has been installed in the building during two years, and the monitoring data have been processed online using MOSS. Three different statistical models have been defined considering the resonant frequencies of the building and the amplitudes of a major crack as estimators. The reported results have shown the potential of MOSS for simultaneously constructing different control charts involving heterogeneous monitoring data. Furthermore, artificial damage scenarios have been included to demonstrate the effectiveness of the proposed automated anomaly detection algorithm for local/global damage detection.

Besides its scientific contribution, the ultimate goal of MOVA/MOSS is also to provide professional engineers with some of the latest state-of-the-art techniques and research breakthroughs in the field of SHM of structures. Moreover, this software is aimed at paving the way for integrated SHM systems with heterogeneous monitoring solutions for local/global damage assessment of civil infrastructure.

Acknowledgement

This work was supported by the Italian Ministry of Education, University and Research (MIUR) through the funded Project of Relevant National Interest "DETECT-AGING - Degradation effects on structural safety of cultural heritage constructions through simulation and health monitoring" (protocol no. 201747Y73L).

References

[1] ASCE, Infrastructure Report Card, ASCE Reston, VA, 2017.

[2] Sustainable Bridges Project, Assessment for Future Traffic Demands and Longer Lives, Doc no. D1. 2 European Railway Bridge Demography, Sixth Framework Program (FP6) of the European Commission (2004).

[3] K. Gkoumas, F. Marques Dos Santos, M. van Balen, A. Tsakalidis, A. Ortega Hortelano, M. Grosso, G. Haq, F. Pekár, Research and Innovation in Bridge Maintenance, Inspection and Monitoring, Technical Report, 2019.

[4] D. Balageas, C. P. Fritzen, A. Güemes, Structural health monitoring, volume 90, John Wiley & Sons, 2010.

[5] C. P. Fritzen, Vibration–based structural health monitoring–concepts and applications, in: Key Engineering Materials, volume 293, Trans Tech Publ, 2005, pp. 3–20.

[6] F. Magalhães, Á. Cunha, Explaining operational modal analysis with data from an arch bridge, Mechanical Systems and Signal Processing 25 (2011) 1431–1450.

[7] E. Reynders, System identification methods for (operational) modal analysis: review and comparison, Archives of Computational Methods in Engineering 19 (2012) 51–124.

[8] W. Soo Lon Wah, Y. T. Chen, G. W. Roberts, A. Elamin, Separating damage from environmental effects affecting civil structures for near real-time damage detection, Structural Health Monitoring 17 (2018) 850–868.

[9] F. Ubertini, N. Cavalagli, A. Kita, G. Comanducci, Assessment of a monumental masonry bell-tower after 2016 Central Italy seismic sequence by long-term SHM, Bulletin of Earthquake Engineering 16 (2018) 775–801.

[10] Q. Sun, W. J. Yan, W. X. Ren, L. L. Liu, Application of transmissibility measurements to operational modal analysis of railway, highway, and pedestrian cable-stayed bridges, Measurement 148 (2019) 106880.

[11] S. Pereira, F. Magalhães, J. P. Gomes, Á. Cunha, J. V. Lemos, Dynamic monitoring of a concrete arch dam during the first filling of the reservoir, Engineering Structures 174 (2018) 548–560.

[12] H. S. Park, B. K. Oh, Real-time structural health monitoring of a supertall building under construction based on visual modal identification strategy, Automation in Construction 85 (2018) 273–289.

[13] S. Diord, F. Magalhães, Á. Cunha, E. Caetano, High spatial resolution modal identification of a stadium suspension roof: Assessment of the estimates uncertainty and of modal contributions, Engineering Structures 135 (2017) 117–135.

[14] K. Soal, Y. Govers, J. Bienert, A. Bekker, System identification and tracking using a statistical model and a kalman filter, Mechanical Systems and Signal Processing 133 (2019) 106127.

[15] D. Uehara, J. Sirohi, Full-field optical deformation measurement and operational modal analysis of a flexible rotor blade, Mechanical Systems and Signal Processing 133 (2019) 106265.

[16] B. J. A. Costa, F. Magalhães, Á. Cunha, J. Figueiras, Rehabilitation assessment of a centenary steel bridge based on modal analysis, Engineering Structures 56 (2013) 260–272.

[17] P. Pachón, R. Castro, E. García-Macías, V. Compan, E. Puertas, E. Torroja's bridge: Tailored experimental setup for SHM of a historical bridge with a reduced number of sensors, Engineering Structures 162 (2018) 11–21.

[18] C. Gentile, M. Guidobaldi, A. Saisi, One-year dynamic monitoring of a historic tower: damage detection under changing environment, Meccanica 51 (2016) 2873–2889.

[19] S. Ivorra, D. Foti, V. Gallo, V. Vacca, D. Bru, Bell's dynamic interaction on a reinforced concrete bell tower, Engineering Structures 183 (2019) 965–975.

[20] C. Gentile, C. Poggi, A. Ruccolo, M. Vasic, Vibration-Based Assessment of the Tensile Force in the Tie-Rods of the Milan Cathedral, International Journal of Architectural Heritage (2019) 1–14.

[21] L. F. Ramos, R. Aguilar, P. B. Lourenço, Operational modal analysis of historical constructions using commercial wireless platforms, Structural Health Monitoring 10 (2011) 511–521.

[22] A. Kita, N. Cavalagli, F. Ubertini, Temperature effects on static and dynamic behavior of Consoli Palace in Gubbio, Italy, Mechanical Systems and Signal Processing 120 (2019) 180–202.

[23] C. Rainieri, G. Fabbrocino, Automated output-only dynamic identification of civil engineering structures, Mechanical Systems and Signal Processing 24 (2010) 678–695.

[24] F. Ubertini, C. Gentile, A. L. Materazzi, Automated modal identification in operational conditions and its application to bridges, Engineering Structures 46 (2013) 264–278.

[25] F. Magalhães, Á. Cunha, E. Caetano, Online automatic identification of the modal parameters of a long span arch bridge, Mechanical Systems and Signal Processing 23 (2009) 316–329.

[26] B. Peeters, G. De Roeck, One–year monitoring of the Z24–Bridge: environmental effects versus damage events, Earthquake engineering & structural dynamics 30 (2001) 149–171.

[27] C. R. Farrar, K. Worden, Structural Health Monitoring.: A Machine Learning Perspective, John Wiley & Sons, 2012.

[28] J. Kullaa, Damage detection of the Z24 bridge using control charts, Mechanical Systems and Signal Processing 17 (2003) 163–170.

[29] A. M. Yan, G. Kerschen, P. De Boe, J. C. Golinval, Structural damage diagnosis under varying environmental conditions–part I: a linear analysis, Mechanical Systems and Signal Processing 19 (2005) 847–864.

[30] A. M. Yan, G. Kerschen, P. De Boe, J. C. Golinval, Structural damage diagnosis under varying environmental conditions–part II: local PCA for non-linear cases, Mechanical Systems and Signal Processing 19 (2005) 865–880.

[31] W. H. Hu, D. H. Tang, J. Teng, S. Said, R. Rohrmann, Structural health monitoring of a prestressed concrete bridge based on statistical pattern recognition of continuous dynamic measurements over 14 years, Sensors 18 (2018) 4117.

[32] A. Elyamani, O. Caselles, P. Roca, J. Clapes, Dynamic investigation of a large historical cathedral, Structural Control and Health Monitoring 24 (2017) e1885.

[33] C. Gentile, A. Ruccolo, F. Canali, Long-term monitoring for the condition-based structural maintenance of the Milan Cathedral, Construction and Building Materials 228 (2019) 117101.

[34] Y. Xia, B. Chen, S. Weng, Y. Q. Ni, Y. L. Xu, Temperature effect on vibration properties of civil structures: a literature review and case studies, Journal of civil structural health monitoring 2 (2012) 29–46.

[35] F. Magalhães, A. Cunha, E. Caetano, Vibration based structural health monitoring of an arch bridge: from automated OMA to damage detection, Mechanical Systems and Signal Processing 28 (2012) 212–228.

[36] M. Regni, D. Arezzo, S. Carbonari, F. Gara, D. Zonta, Effect of environmental conditions on the modal response of a 10-story reinforced concrete tower, Shock and Vibration 2018 (2018).

[37] Y. Zhou, L. Sun, Insights into temperature effects on structural deformation of a cable-stayed bridge based on structural health monitoring, Structural Health Monitoring 18 (2019) 778–791.

[38] E. Reynders, M. Schevenels, G. De Roeck, Macec 3.2: A matlab toolbox for experimental and operational modal analysis-user's manual, Katholieke Universiteit, Leuven (2011).

[39] L. M. S. Test, Lab modal analysis user manual, Siemens Industry Software NV (2015).

[40] SVS, ARTeMIS Extractor Pro User's Manual, Release 3.5, Structural Vibration Solutions, Aalborg, Denmark, 2006.

[41] I. Catapano, G. Ludeno, F. Soldovieri, F. Tosti, G. Padeletti, Structural assessment via ground penetrating radar at the Consoli Palace of Gubbio (Italy), Remote Sensing 10 (2018) 45.

[42] N. Cavalagli, A. Kita, V. L. Castaldo, A. L. Pisello, F. Ubertini, Hierarchical environmental risk mapping of material degradation in historic masonry buildings: An integrated approach considering climate change and structural damage, Construction and Building Materials 215 (2019) 998–1014.

[43] G. Comanducci, F. Magalhães, F. Ubertini, Á. Cunha, On vibration-based damage detection by multivariate statistical techniques: Application to a long-span arch bridge, Structural health monitoring 15 (2016) 505–524.

[44] E. García-Macías, A. Kita, F. Ubertini, Synergistic application of operational modal analysis and ambient noise deconvolution interferometry for structural and damage identification in historic masonry structures: three case studies of Italian architectural heritage, Structural Health Monitoring (2019) 1475921719881450.

[45] C. Rainieri, G. Fabbrocino, Operational modal analysis of civil engineering structures, Springer, New York 142 (2014) 143.

[46] J. N. Juang, Applied system identification, Prentice-Hall, Inc., Englewood Cliffs, NJ, USA, 1994.

[47] R. Brincker, L. Zhang, P. Andersen, Modal identification of output-only systems using frequency domain decomposition, Smart materials and structures 10 (2001) 441.

[48] S. R. Ibrahim, The experimental determination of vibration parameters from time responses, Shock Vibration Bull. 46 (1976) 187–196.

[49] B. Peeters, H. Van der Auweraer, PolyMAX: a revolution in operational modal analysis, in: Proceedings of the 1st International Operational Modal Analysis Conference, Copenhagen, Denmark, pp. 26–27.

[50] E. Reynders, G. De Roeck, G. Degrande, System identification and modal analysis in structural mechanics, in: National Congress on Theoretical and Applied Mechanics, Date: 2012/05/09-2012/05/10, Location: Brussels, Belgium.

[51] P. Van Overschee, B. L. De Moor, Subspace identification for linear systems: Theory–Implementation–Applications, Kluwer Academic Publishers, Dordrecht, 1996.

[52] B. Peeters, System identification and damage detection in civil engeneering, Ph.D. thesis, KU Leuven, 2000.

[53] F. Magalhães, Operational modal analysis for testing and monitoring of bridges and special structures, Ph.D. thesis, University of Porto, 2010.

[54] H. Hotteling, Multivariate quality control, illustrated by the air testing of sample bombsights, Techniques of statistical analysis (1947) 111–184.

[55] R. B. Crosier, Multivariate generalizations of cumulative sum quality-control schemes, Technometrics 30 (1988) 291–303.

[56] C. A. Lowry, W. H. Woodall, C. W. Champ, S. E. Rigdon, A multivariate exponentially weighted moving average control chart, Technometrics 34 (1992) 46–53.

[57] R. Killick, P. Fearnhead, I. A. Eckley, Optimal detection of changepoints with a linear computational cost, Journal of the American Statistical Association 107 (2012) 1590–1598.

[58] Y. Yang, S. Nagarajaiah, Blind denoising of structural vibration responses with outliers via principal component pursuit, Structural Control and Health Monitoring 21 (2014) 962–978.

[59] F. Ubertini, G. Comanducci, N. Cavalagli, A. L. Pisello, A. L. Materazzi, F. Cotana, Environmental effects on natural frequencies of the San Pietro bell tower in Perugia, Italy, and their removal for structural performance assessment, Mechanical Systems and Signal Processing 82 (2017) 307–322.

[60] W. S. L. Wah, J. S. Owen, Y. T. Chen, A. Elamin, G. W. Roberts, Removal of masking effect for damage detection of structures, Engineering Structures 183 (2019) 646–661.